

# Eddington Ratios of Dust-obscured Quasars at $z \lesssim 1$ : Evidence Supporting Dust-obscured Quasars as Young Quasars

Dohyeong Kim<sup>1</sup>, Yongjung Kim<sup>2</sup>, Myungshin Im<sup>3</sup>, Eilat Glikman<sup>4</sup>, Minjin Kim<sup>5</sup>, Tanya Urrutia<sup>6</sup>, and Gu Lim<sup>1</sup>

<sup>1</sup> Department of Earth Sciences, Pusan National University, Busan 46241, Republic of Korea

<sup>2</sup> Korea Astronomy and Space Science Institute, Daejeon 34055, Republic of Korea

<sup>3</sup> SNU Astronomy Research Center (SNU ARC), Astronomy Program, Dept. of Physics & Astronomy, Seoul National University, Seoul 08826, Republic of Korea

<sup>4</sup> Department of Physics, Middlebury College, Middlebury, VT 05753, USA

<sup>5</sup> Department of Astronomy and Atmospheric Sciences, College of Natural Sciences, Kyungpook National University, Daegu 41566, Republic of Korea

<sup>6</sup> Leibniz-Institut für Astrophysik, Potsdam (AIP), An der Sternwarte 16, 14482 Potsdam, Germany  
e-mail: dh.dr2kim@gmail.com; yjkim.ast@gmail.com

–; –

## ABSTRACT

Dust-obscured quasars have been suspected as the intermediate stage galaxies between merger-driven star-forming galaxies and unobscured quasars. This merger-driven galaxy evolution scenario suggests that dust-obscured quasars exhibit higher Eddington ratios ( $\lambda_{\text{Edd}}$ ) than those of unobscured quasars. However, their high dust obscuration poses challenges to accurately measuring their  $\lambda_{\text{Edd}}$  using commonly employed bolometric luminosity ( $L_{\text{bol}}$ ) and black hole (BH) mass ( $M_{\text{BH}}$ ) estimators based on the ultraviolet (UV) or optical luminosity. Recently, Kim et al. (2023) established new estimators for  $L_{\text{bol}}$  and  $M_{\text{BH}}$  based on mid-infrared (MIR) continuum luminosity ( $L_{\text{MIR}}$ ), which are less affected by dust obscuration. These estimators enable the study of a large number of dust-obscured quasars across a wide redshift range. In this study, we measure the  $\lambda_{\text{Edd}}$  values of 30 dust-obscured quasars at  $z \lesssim 1$ , the largest sample size to date, using the  $L_{\text{MIR}}$ -based  $L_{\text{bol}}$  and  $M_{\text{BH}}$  estimators. Our findings reveal that dust-obscured quasars exhibit significantly higher  $\lambda_{\text{Edd}}$  values compared to unobscured quasars. Moreover, we confirm that the enhanced  $\lambda_{\text{Edd}}$  values of dust-obscured quasars maintain consistency across the redshift span of 0 to 1. Our results strongly support the picture that dust-obscured quasars are in the earlier stage than unobscured quasars in the merger-driven galaxy evolutionary track.

**Key words.** Galaxies: active – (Galaxies:) quasars: general – (Galaxies:) quasars: supermassive black holes – (Galaxies:) quasars: emission lines – Galaxy: evolution – Infrared: galaxies

## 1. Introduction

Quasars are one of the most energetic and luminous objects in the universe, and they emit the enormous energy in all wavelengths from gamma-ray to radio. The energy of quasars is powered by the accretion of surrounded materials onto supermassive black holes (SMBHs). These SMBHs are found at the centers of massive spheroidal galaxies, and the BH masses have correlations with several properties of host galaxies (e.g., Ferrarese & Merritt 2000; Gebhardt et al. 2000).

To date, almost million quasars have been found based on X-ray, UV, optical, and radio surveys (Grazian et al. 2000; Becker et al. 2001; Anderson et al. 2003; Croom et al. 2004; Risaliti & Elvis 2005; Schneider et al. 2005; Véron-Cetty & Véron 2006; Young et al. 2009; Pâris et al. 2014; Kim et al. 2015, 2019, 2020; Lyke et al. 2020; Shin et al. 2020; Kim et al. 2022; Shin et al. 2022). However, some previous studies (e.g., Comastri et al. 2001; Tozzi et al. 2006; Polletta et al. 2008) reported that soft X-ray, UV, and optical quasar surveys may overlook a substantial number of quasars, which have red colors caused by the dust extinction from intervening dust and gas in their host galaxies (Webster et al. 1995; Cutri et al. 2002) or our galaxy (Im et al. 2007; Lee et al. 2008). In this paper, we refer to the quasars with the dust extinction from their host galaxies as dust-obscured quasars. Some previous studies (e.g., Polletta et al. 2008) ex-

pected that these dust-obscured quasars could make up ~50 % of the whole quasar population, and even the optical quasar surveys include a considerable number of dust-obscured quasars (e.g., ~15 %; Kim et al. 2023).

Dust-obscured quasars have been found through various methods, but the use of their red colors is a notably useful technique. Especially, the colors in near-infrared (NIR; e.g.,  $J - K > 2$  mag; Cutri et al. 2001, 2002) and optical through NIR (e.g.,  $R - K > 5$  mag and  $J - K > 1.3$  mag; Glikman et al. 2007; Urrutia et al. 2009) have been widely used. The quasars found by these red colors are called red quasars, and using these red colors proves to be an effective way to find dust-obscured quasars since the red colors of most red quasars originate from the dust extinction (Kim & Im 2018). However, Kim et al. (2018) claimed that using only NIR color is not effective in selecting dust-obscured quasars.

Although our knowledge about dust-obscured quasars is still incomplete, the emergence of dust-obscured quasars is commonly associated with a merger-driven galaxy evolution scenario, extensively explored in previous simulation studies (Menci et al. 2004; Hopkins et al. 2005, 2006, 2008). In this merger-driven galaxy evolution scenario, major mergers between gas-rich galaxies can trigger both star-formation and BH activities, and these phase galaxies are often seen as

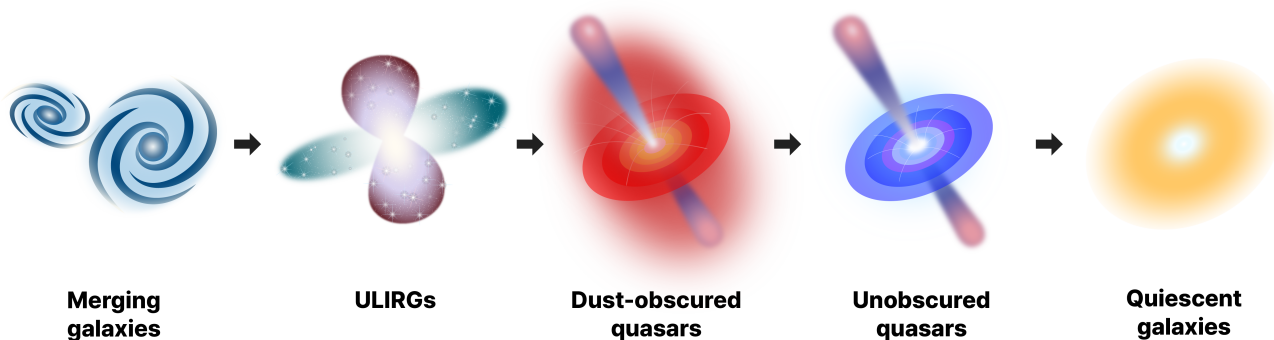


**Fig. 1.** Schematic outline of merger-driven galaxy evolution scenario.

ultra-luminous infrared galaxies (ULIRGs; Sanders et al. 1988; Sanders & Mirabel 1996). After this phase, these galaxies can have merging features and star-formation activities. Furthermore, since gas flows onto the SMBHs are related to galaxy-scale disturbances caused by galaxy merger-driven torques (Di Matteo et al. 2005; Hopkins et al. 2008; Alexander & Hickox 2012), it is expected that their BH activities increase dramatically, resulting in the emitting enormous amounts of energy with a high  $\lambda_{\text{Edd}}$ . However, their BH activities are still obscured owing to the remaining dust and gas in their host galaxies. Finally, these galaxies evolve to normal unobscured quasars after sweeping away the remaining dust and gas by quasar-driven winds. Figure 1 shows a schematic outline of this merger-driven galaxy evolution scenario.

In this scenario, it is believed that dust-obscured quasars can occur as the intermediate stage galaxies between the merger-driven star-forming galaxies and unobscured quasars. Several theoretical studies (e.g., Hopkins et al. 2008) have suggested that dust-obscured quasars exhibit high BH accretion rates, which appear to be prevalent. This scenario has been supported by several pieces of observational evidence. For example, dust-obscured quasars have (i) high  $\lambda_{\text{Edd}}$  values (Urrutia et al. 2012; Kim et al. 2015a, 2018, 2024), (ii) high fractions of merging features in their host galaxies (Urrutia et al. 2008; Glikman et al. 2015), (iii) dusty red colors (Kim & Im 2018), (iv) merging SMBH systems (Kim et al. 2020), and (v) enhanced star-formation activities (Georgakakis et al. 2009).

Note, however, that even in the merger-driven galaxy evolution scenario, the properties of dust-obscured quasars remain controversial. Recently, Lansbury et al. (2020) showed that the dust-obscured quasar phase lasts a few  $10^5$  years, which is significantly shorter than quasar lifetime of  $\sim 10^7$  years (e.g., Hopkins et al. 2006; Khrykin et al. 2021). Considering this significantly short dusty phase, some unobscured quasars might have SMBHs as active as those in dust-obscured quasars. However, these lifetimes are sensitive to several properties (e.g.,  $L_{\text{bol}}$  and stellar mass; Hopkins et al. 2006), and hence more extensive observational studies on the quasar lifetimes are necessary to obtain a conclusive understanding of the BH activities of dust-obscured quasars. Moreover, some recent studies (e.g., Jun et al. 2021; Glikman et al. 2024) showed that outflows slowly sweep-

ing away the dust and gas in host galaxies could result in luminous dust-obscured quasars with enhanced BH activities.

Alternative explanation for dust-obscured quasars is that they are obscured by a dust torus. The unification model suggests that the differences in emission lines between type 1 and 2 active galactic nuclei are due to the viewing angle (Antonucci 1993; Urry & Padovani 1995). Some previous studies (e.g., Wilkes et al. 2002; Rose et al. 2013; Ananna et al. 2022a,b) proposed that the red colors can be a result of moderate viewing angle in the unification model, where dust torus blocks the photon from accretion disk and broad line region (BLR), instead of the dust and gas in their host galaxies. In this scenario, dust-obscured quasars appear solely due to the viewing angle, so their BH accretion rates should not differ from those of unobscured quasars. Even when considering the dust torus evolution with BH accretion rates (Ananna et al. 2022a,b), a significant number of dust-obscured quasars are expected to exhibit lower BH accretion rates than unobscured quasars.

Another possible explanation for dust-obscured quasars is that strong outflows play a crucial role in transporting the obscuring medium (Calistro Rivera et al. 2021). Several observational studies showed that dust-obscured quasars exhibit strong outflows (e.g., Lansbury et al. 2020; Stacey et al. 2022; Glikman et al. 2024), which support this explanation. Note, however, that strong outflows are also expected to occur in the intermediate stage galaxies of the merger-driven galaxy evolution scenario, indicating that it cannot be considered a completely separate explanation from the merger-driven galaxy evolution scenario.

Furthermore, some previous studies (e.g., Puchnarewicz & Mason 1998; Whiting et al. 2001; Rose 2014) suggested that red quasars have intrinsic red colors, instead of the dust extinction. Additionally, Georgantopoulos et al. (2023) demonstrated that red quasars reside in the galaxies located between the young and old galaxy populations, in contrast to expectations from the merger-driven galaxy evolution scenario.

One of the ways to confirm if dust-obscured quasars are the intermediate population under the merger-driven galaxy evolution scenario is to examine whether dust-obscured quasars have high  $\lambda_{\text{Edd}}$  values. However, the  $\lambda_{\text{Edd}}$  values of dust-obscured quasars remain a topic of debate due to that most of bolometric luminosity and BH mass estimators are established based on UV or optical luminosity (Kaspi et al. 2000; Vestergaard 2002;

McLure & Dunlop 2004; Greene & Ho 2005), where the UV- and optical-based estimators are easily affected by the dust extinction. For example, if a dust-obscured quasar is obscured by a color excess of  $E(B - V) = 2$  mag, its fluxes at 1450 Å and 5100 Å are suppressed by factors of  $4.3 \times 10^6$  and 500, respectively, which is obtained from a reddening law (Fitzpatrick 1999) with  $R_V = 3.1$  (Weingartner & Draine 2001). Furthermore, to determine the  $E(B - V)$  values for dust-obscured quasars is also uncertain; the differences in  $E(B - V)$  estimates can vary as much as 1–2 mag, depending on the method used (Glikman et al. 2007; Urrutia et al. 2012; Kim et al. 2018). If a dust-obscured quasar with a color excess of  $E(B - V) = 1$  mag is measured as having  $E(B - V) = 2$  mag, then its fluxes at 1450 Å and 5100 Å are overestimated by  $\sim 2000$  and  $\sim 20$  times, respectively, after correcting the dust extinction. Recently, Calistro Rivera et al. (2021) measured the  $\lambda_{\text{Edd}}$  values of  $\sim 300$  dust-obscured quasars using UV and optical luminosities, and found no significant difference from those of unobscured quasars. However, Calistro Rivera et al. (2021) used UV and optical luminosities to measure the BH properties, which are sensitive to accuracy in  $E(B - V)$  measurements.

To overcome the limitations of the UV- and optical-based estimators, several infrared (IR)-based estimators have been established. If a dust-obscured quasar with  $E(B - V) = 1$  mag is incorrectly measured as  $E(B - V) = 2$  mag, then the dust extinction corrected fluxes of Pa $\alpha$  (1.87  $\mu\text{m}$ ) and Br $\alpha$  (4.05  $\mu\text{m}$ ) lines would be overestimated by only a factor of 1.48 and 1.16, respectively. For this advantage, Paschen and Brackett hydrogen line based estimators were derived (e.g., Kim et al. 2010, 2015b, 2022). However, despite the advantage, these IR-based estimators need IR spectroscopic observation, and applying them to a large number of dust-obscured quasars has been a tough task due to the difficulty in obtaining IR spectroscopic data. Consequently, while several previous studies (Kim et al. 2015a; Kim & Im 2018; Kim et al. 2018) showed that the  $\lambda_{\text{Edd}}$  values of dust-obscured quasars are higher than those of unobscured quasars using these IR-based estimators, they used the limited sample size ( $\leq 15$ ), yielding the results are (i) not statistically robust and (ii) not confirmed for a wide redshift range.

Recently, Kim et al. (2023) established bolometric luminosity and BH mass estimators based on  $L_{\text{MIR}}$  using 129 unobscured ( $E(B - V) < 0.1$ ) Sloan Digital Sky Survey (SDSS; York et al. 2000) quasars at  $z \lesssim 0.5$ . The  $L_{\text{MIR}}$  values can be derived via spectral energy distribution (SED) fitting using various photometric data, such as SDSS (York et al. 2000), Two Micron All-Sky Survey (2MASS; Skrutskie et al. 2006), and Wide-field Infrared Survey Explorer (WISE; Wright et al. 2010). The bolometric luminosity can be measured from the  $L_{\text{MIR}}$  with an rms scatter of  $\sim 0.1$  dex, while the BH mass can be derived with an rms scatter of  $\leq 0.2$  dex using the  $L_{\text{MIR}}$  with the FWHM of Balmer lines. Since the measurement of the FWHM of Balmer lines is not significantly affected by the dust extinction, the  $L_{\text{MIR}}$ -based estimators allow for the determination of  $L_{\text{bol}}$  and  $M_{\text{BH}}$  without the need for IR spectroscopic data and relatively unaffected by the dust extinction. Hence, these  $L_{\text{MIR}}$ -based estimators can be applied for a large number of dust-obscured quasars, and they are expected to yield the statistically robust result of the  $\lambda_{\text{Edd}}$  values of dust-obscured quasars.

In this paper, we measure the  $\lambda_{\text{Edd}}$  values of 30 dust-obscured quasars at  $z \lesssim 1$  using the  $L_{\text{MIR}}$ -based estimators (Kim et al. 2023), and compare them to unobscured quasars selected from the SDSS quasars. Throughout this work, we use a standard  $\Lambda\text{CDM}$  model of  $H_0 = 70 \text{ km s}^{-1} \text{ Mpc}^{-1}$ ,  $\Omega_m = 0.3$ , and

$\Omega_\Lambda = 0.7$ . This model has been supported by observational studies in the past decades (e.g. Im et al. 1997; Planck Collaboration et al. 2016).

## 2. Sample

Our sample is drawn from 120 dust-obscured quasars listed in Glikman et al. (2012), and these dust-obscured quasars were selected via the following procedures. First, they selected dust-obscured quasar candidates using (i) detections in NIR (2MASS Point Source Catalog [PSC]; Cutri et al. 2003) and radio (Faint Images of the Radio Sky at Twenty-centimeters [FIRST]; Becker et al. 1995); and (ii) red colors in NIR ( $J - K > 1.7$  mag) and optical through NIR ( $R - K > 4$  mag). Through this process, a total of 395 dust-obscured quasar candidates were selected. Second, Glikman et al. (2012) obtained the optical and/or NIR spectra of  $\sim 300$  dust-obscured quasar candidates for (i) object identification; (ii) redshift determination; and (iii) dust reddening determination. Finally, of the  $\sim 300$  candidates, they found 120 dust-obscured quasars having  $E(B - V) > 0.1$ , and provide their optical and/or NIR spectra.

Among the 120 dust-obscured quasars, we select 30 dust-obscured quasars at  $z \lesssim 1$  by following conventions. First, broad component of H $\beta$  or H $\alpha$  line is broader than  $2000 \text{ km s}^{-1}$  (see Section 3.1 for more details). Second,  $E(B - V)$  measured from spectral energy distribution (SED) fitting is greater than 0.1, and the details of the SED fitting procedure are described in Section 3.2. Third, quasar fractions at 3.4  $\mu\text{m}$  and 4.6  $\mu\text{m}$  determined by the SED fitting exceed 0.5. The definition of the quasar fraction is also provided in Section 3.2.

The selected 30 dust-obscured quasars span over wide ranges of BH mass ( $10^{8.15} M_\odot < M_{\text{BH}} < 10^{9.22} M_\odot$ ), bolometric luminosity ( $10^{44.94} \text{ erg s}^{-1} < L_{\text{bol}} < 10^{47.07} \text{ erg s}^{-1}$ ), and redshift ( $0.137 < z < 0.957$ ), where the BH masses and bolometric luminosities are derived using  $L_{\text{MIR}}$ -based-estimators (Kim et al. 2010, 2023). Their basic properties are shown in Figure 2.

In order to compare the dust-obscured quasars to unobscured quasars, we select unobscured quasars from SDSS Data Release 14 (DR14) quasar catalog (P aris et al. 2018). This catalog contains 526,265 quasars, and their spectral properties were measured (Rakshit et al. 2020) by performing multi-component fitting with PyQSOFit code (Guo et al. 2019; Shen et al. 2019). To avoid sample bias effects, we choose the SDSS quasars with the same selection criteria of the dust-obscured quasars: (i) redshift range of  $0.137 < z < 0.957$ ; (ii) FIRST radio detection; (iii) detections in the  $J$ -,  $H$ -, and  $K$ -bands from 2MASS PSC; and (iv) quasar fractions at 3.4  $\mu\text{m}$  and 4.6  $\mu\text{m}$  from the SED fitting exceed 0.5.

Moreover, while SDSS quasars are generally known to have negligible dust extinction, Kim et al. (2023) and Y. Kim et al. (2024) showed that a significant fraction ( $\sim 10$ – $15$  %) of SDSS quasars are affected by dust extinction. Therefore, we perform the SED fitting (See Section 3.2) on SDSS quasars and include only those samples with the measured  $E(B - V) < 0.1$ . These SDSS quasars with  $E(B - V) < 0.1$  can be classified as unobscured quasars. Kim et al. (2023) showed that the low  $E(B - V)$  SDSS quasars exhibit similar Balmer decrement of unobscured quasars (Dong et al. 2008), supporting the classification of these SDSS quasars with low  $E(B - V)$  as unobscured.

Using these selection criteria, 614 SDSS quasars are chosen. Figure 2 shows the  $L_{4.6-z}$  distributions of the dust-obscured quasars and the selected SDSS quasars. The dust-obscured quasars tend to be slightly brighter than the SDSS quasars at a given redshift, which may cause a sample bias. To eliminate

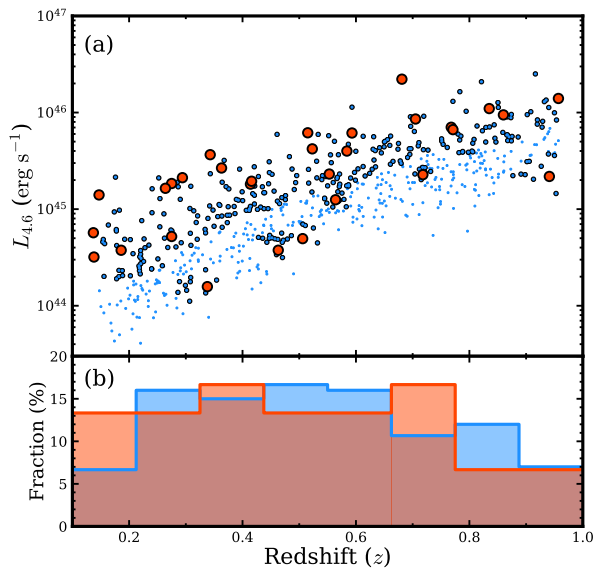


**Fig. 2.** (a) Redshift versus  $L_{4,6}$  luminosity. Red circles and blue dots denote the selected dust-obscured quasars and SDSS quasars, respectively. Among the blue dots, 300 blue dots with black edges represent the  $L_{4,6}$ - $z$  matched SDSS quasars, which are used as unobscured quasars. (b) Redshift distributions of the two kinds of quasars. Red and blue histograms represent the dust-obscured quasars and the unobscured quasars, respectively.

this effect, we select the 10 closest SDSS quasars to each dust-obscured quasar using a two-dimensional metric on the  $L_{4,6}$  and redshift space. If an SDSS quasar was already selected for another nearby dust-obscured quasar, we excluded it and selected the next closest SDSS quasar.

Finally, 300 SDSS quasars with similar  $L_{4,6}$  values and redshifts to the selected 30 dust-obscured quasars are found and used as unobscured quasars. The unobscured quasars have a wide range of BH mass ( $10^{7.76} M_{\odot} < M_{\text{BH}} < 10^{10.03} M_{\odot}$ ), bolometric luminosity ( $10^{44.79} \text{ erg s}^{-1} < L_{\text{bol}} < 10^{47.12} \text{ erg s}^{-1}$ ), and redshift ( $0.154 < z < 0.954$ ). Naturally, their  $K$ -band magnitudes and redshift distributions are comparable to those of the dust-obscured quasars, as shown in Figure 2.

### 3. Analysis

#### 3.1. Spectral Fitting of Balmer Lines

In this subsection, we describe how  $\text{H}\beta$  and  $\text{H}\alpha$  lines of the dust-obscured quasars are fitted to measure FWHM values for broad components of the Balmer lines, and the FWHM values are used for estimating BH masses of the dust-obscured quasars. For this analysis, we use the optical and/or NIR spectra provided by Glikman et al. (2012). However, note that the FWHM values of the unobscured quasars are adopted from Rakshit et al. (2020).

To fit the Balmer lines of the dust-obscured quasars, we use the PyQSOFit code for consistency in methodology, which is identical to the procedure for the unobscured quasars (Rakshit et al. 2020). Using the PyQSOFit code, we decompose several components of host galaxy, power-law continuum, and Fe II emissions from the spectra. After that, we fit the Balmer lines. We fit  $\text{H}\beta$  and  $\text{H}\alpha$  line complexes separately, while all emission

lines in each line complex are fitted simultaneously. Note that the  $\text{H}\beta$  line complex includes  $\text{H}\beta$  (broad and narrow components) and  $[\text{O III}] \lambda\lambda 4959, 5007$  doublet (core and wing components), and the  $\text{H}\alpha$  line complex comprises  $\text{H}\alpha$  (broad and narrow components),  $[\text{N II}] \lambda\lambda 6549, 6585$  doublet, and  $[\text{S II}] \lambda\lambda 6718, 6732$  doublet. Although the flux ratios of these doublets are fixed, we fit the Balmer line complexes without fixing the flux ratios due to low S/N and partially truncated spectra. We find that not fixing the flux ratios has a negligible effects on the FWHM measurements of the broad components of the Balmer lines.

During the fitting, the broad components of the Balmer lines are fitted with a single- or multiple-Gaussian model. However, the FWHM values estimated by the single-Gaussian model is systematically different from the FWHM values from the multi-Gaussian model (Kim et al. 2010; Shen et al. 2011). Thus, we apply correction factors (Kim et al. 2010) to remove the model bias, which are derived from well-resolved Balmer lines of 26 unobscured bright quasars at low- $z$ . For the broad components, we set a lower limit of the FWHM as  $2000 \text{ km s}^{-1}$ , and this FWHM criterion for the broad components has been widely used (e.g., Suh et al. 2019; Xu et al. 2007). The FWHM criterion, broader than that used in Glikman et al. (2012), is set to exclude narrow line Seyfert 1 galaxies (e.g.,  $\text{FWHM} \lesssim 2000 \text{ km s}^{-1}$ ; Zhou et al. 2006) that may have systematically different  $\lambda_{\text{Edd}}$  values (Boroson 2002). Moreover, we only use the FWHM values that are measured reliably, selecting those with a  $\text{FWHM}/\text{FWHM}_{\text{fit\_err}}$  of greater than 3, where  $\text{FWHM}_{\text{fit\_err}}$  represents the error in FWHM from the fitting.

Through this process, we fit the spectra of 120 dust-obscured quasars in Glikman et al. (2012), ultimately selecting 30 objects with reliably measured FWHM values. Figure 3 shows the line fitting results. The fit provides the FWHM values of the broad components of the Balmer lines, but we use the FWHM values after correcting instrumental wavelength dispersion as  $\text{FWHM}^2 = (\text{FWHM}_{\text{fit}})^2 - (\text{FWHM}_{\text{inst}})^2$ , where  $\text{FWHM}_{\text{fit}}$  and  $\text{FWHM}_{\text{inst}}$  denote the FWHM provided from the fit and the wavelength dispersion due to the instrumental spectral resolution, respectively. In this work, we use the corrected FWHM values of the Balmer lines, and they are summarized in Table 1. Note that to avoid the effects of correction bias, the same instrumental wavelength dispersion correction is also applied to the FWHM values of unobscured quasars adopted from Rakshit et al. (2020), and the corrected FWHM values are used in this study.

We validate the accuracy of our FWHM measurements through two methods: (i) by comparing them with the well-established relationship between Balmer lines; (ii) by cross-referencing with individual measurements from previous studies. Among the 30 dust-obscured quasars, the fit provides the FWHM values for both the  $\text{H}\beta$  and  $\text{H}\alpha$  lines in six objects. Our FWHM measurements for the Balmer lines are consistent with the well-known relationship,  $\log\left(\frac{\text{FWHM}_{\text{H}\beta}}{\text{km s}^{-1}}\right) = 0.103 + \log\left(\frac{\text{FWHM}_{\text{H}\alpha}}{\text{km s}^{-1}}\right)$ , established by Bisogni et al. (2017), as shown in Figure 4. Additionally, seven dust-obscured quasars were studied in Urrutia et al. (2012), and their Balmer line FWHM values were measured. Among these objects, three have their  $\text{FWHM}_{\text{H}\beta}$  values measured in both this work and Urrutia et al. (2012), while another three objects have  $\text{FWHM}_{\text{H}\alpha}$  values measured in both studies. For the remaining object,  $\text{FWHM}_{\text{H}\alpha}$  is measured in this work, whereas Urrutia et al. (2012) measured  $\text{FWHM}_{\text{H}\beta}$ . For this object, we convert the  $\text{FWHM}_{\text{H}\beta}$  to  $\text{FWHM}_{\text{H}\alpha}$  using the relationship established by Bisogni et al. (2017) for comparison. Comparing the FWHM values measured in both stud-

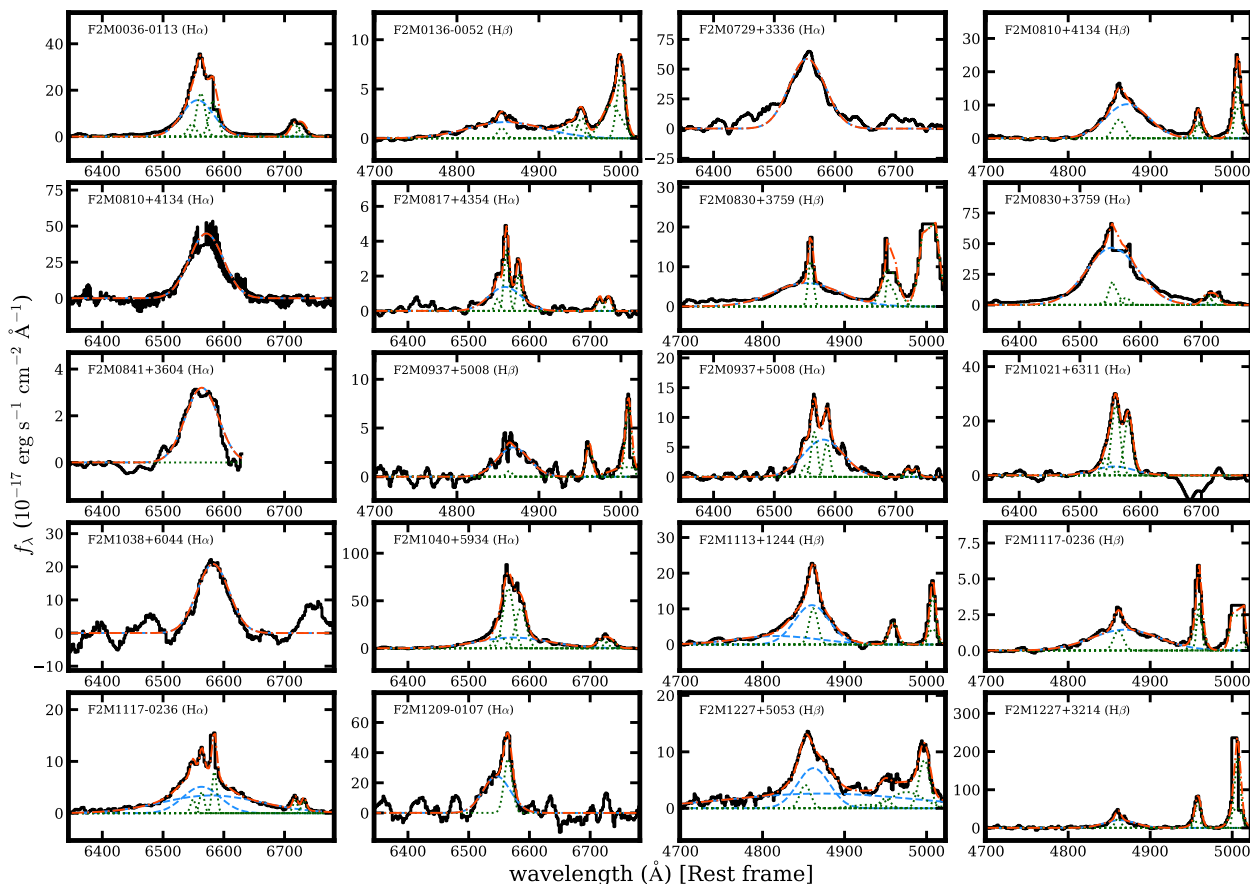


**Fig. 3.** The fitting results of the H $\beta$  and H $\alpha$  lines for the dust-obscured quasars. The black solid lines denote the continuum-subtracted spectra in the rest-frame. The red dash-dotted lines are the best-fit model, and the blue dashed and green dotted lines represent the broad and narrow components of the each line complex, respectively.

ies reveals that, although not perfectly aligned, they closely match for most objects, with only a few exceptions. Upon selecting only those samples whose both FWHM measurements are over  $2000 \text{ km s}^{-1}$ , the rms scatter between the FWHM measurements is 0.12 dex, which is taken as the average FWHM error ( $\text{FWHM}_{\text{avg\_err}}$ ). The total error in FWHM ( $\text{FWHM}_{\text{tot\_err}}$ ) is taken as the square root of the quadratic sum of the fitting error and average error as  $\text{FWHM}_{\text{tot\_err}}^2 = \text{FWHM}_{\text{fit\_err}}^2 + \text{FWHM}_{\text{avg\_err}}^2$ . However, the measured rms scatter is significantly affected by a few samples with the large discrepancies in FWHM measurements, suggesting the possibility that the rms scatter could be overestimated. Note that the exceptions are related to the  $\text{FWHM}_{\text{H}\alpha}$  measurements, which implies that the possibility of inaccuracy in the  $\text{FWHM}_{\text{H}\alpha}$  measurements cannot be ruled out. These comparisons of the FWHM values are shown in Figure 4, suggesting the reliability of our FWHM measurements.

### 3.2. SED Fitting for MIR Continuum Luminosities

In order to measure  $L_{\text{bol}}$  and  $M_{\text{BH}}$  values of the dust-obscured and the unobscured quasars using the  $L_{\text{MIR}}$ -based estimators (Kim et al. 2023), we estimate monochromatic continuum luminosity,  $\lambda L_{\lambda}$ , at  $3.4 \mu\text{m}$  and  $4.6 \mu\text{m}$  (hereafter,  $L_{3.4}$  and  $L_{4.6}$ , respectively) in the rest-frame. Although Kim et al. (2023) showed that host galaxy contaminations at  $3.4 \mu\text{m}$  and  $4.6 \mu\text{m}$  are negli-

ble ( $< 20\%$ ), we measure the  $L_{3.4}$  and  $L_{4.6}$  values after subtracting the host galaxy light by an SED fitting with optical-to-MIR photometric data of SDSS, 2MASS PSC, and WISE. For these photometric data, the intrinsic fluctuation ( $\sigma_m = 0.035 \text{ mag}$ ) of the spectrum with respect to a simple power-law spectrum found in Kim et al. (2015b) is added in quadrature to the original photometric error in each band. Note that we additionally use  $B$ - and  $R$ -band photometry (Lasker et al. 2008) adopted from Glikman et al. (2012) for only the dust-obscured quasars.

The SED fitting is implemented using the method described in Kim et al. (2023). The photometric data, denoted as  $f(\lambda)$ , are fitted with an SED model that combines quasar ( $Q(\lambda)$ ), elliptical galaxy ( $E(\lambda)$ ), spiral galaxy ( $S(\lambda)$ ), and irregular galaxy ( $I(\lambda)$ ) spectra through a weighted sum, as

$$f(\lambda) = C_1 Q(\lambda) + C_2 E(\lambda) + C_3 S(\lambda) + C_4 I(\lambda), \quad (1)$$

where  $C_1$ ,  $C_2$ ,  $C_3$ , and  $C_4$  are the normalization constants. Note that the  $Q(\lambda)$ ,  $E(\lambda)$ ,  $S(\lambda)$ , and  $I(\lambda)$  are reddened spectra of  $Q_0(\lambda)$ ,  $E_0(\lambda)$ ,  $S_0(\lambda)$ , and  $I_0(\lambda)$ , respectively. The  $Q_0(\lambda)$  spectrum is adopted from Krawczyk et al. (2013), while the  $E_0(\lambda)$ ,  $S_0(\lambda)$ , and  $I_0(\lambda)$  spectra are taken from Assef et al. (2010). The intrinsic quasar spectrum of Krawczyk et al. (2013) is not significantly different from other quasar spectral templates (e.g., Richards et al. 2006; Assef et al. 2010) in the optical-to-MIR wavelength range (Kim et al. 2023).



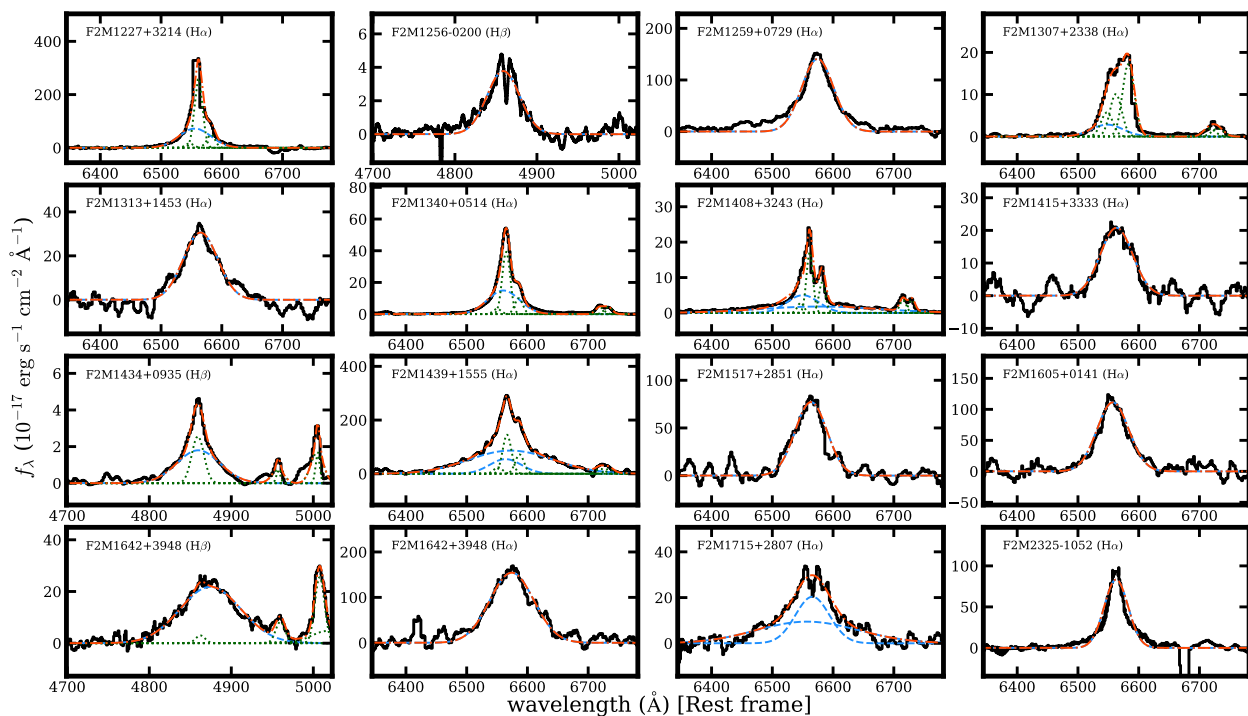
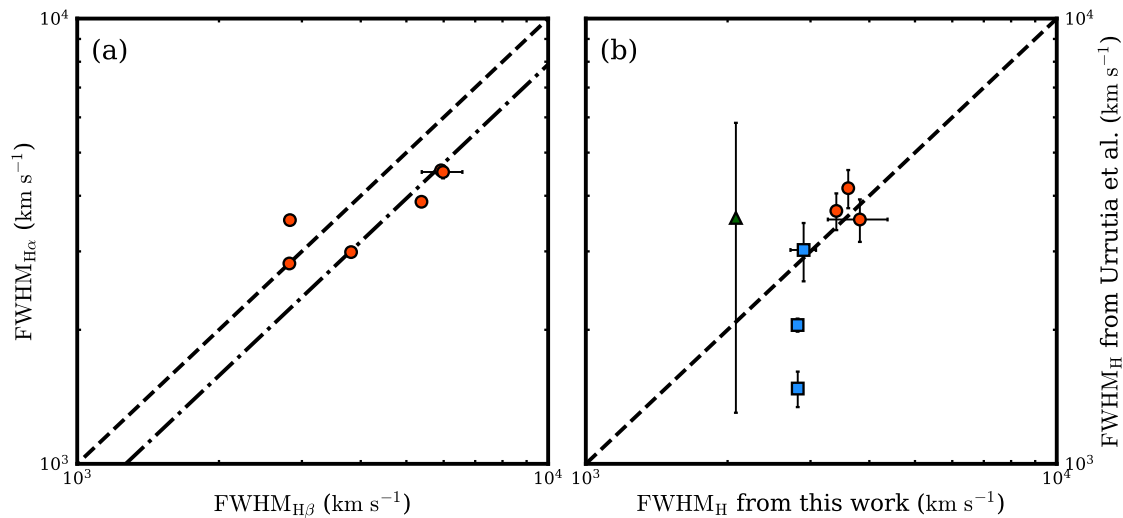


Fig. 3. Continued.



**Fig. 4.** (a) Comparison of FWHM values of broad components of  $H\beta$  and  $H\alpha$  lines. The dashed line denotes a line where the FWHM values of the Balmer lines are identical, and dash-dotted line is a well-known relationship between the FWHM values of the Balmer lines (Bisogni et al. 2017). (b) Comparison of Balmer line FWHM values measured from this work and Urrutia et al. (2012). Red circles denote the comparison of  $\text{FWHM}_{H\beta}$  measurements, and blue squares mean the comparison of  $\text{FWHM}_{H\alpha}$  measurements. Green triangles represent the  $\text{FWHM}_{H\alpha}$  measurement comparison, but the  $\text{FWHM}_{H\beta}$  measured in Urrutia et al. (2012) is converted to the  $\text{FWHM}_{H\alpha}$  using the relationship established in Bisogni et al. (2017). The meaning of dashed line is identical to that of the panel (a).

For the dust reddening, we adopt a reddening law of Fitzpatrick (1999) based on average Galactic extinction curve with an assumption of  $R_V = 3.1$  (e.g., Weingartner & Draine 2001). Note that the reddening law is significantly different from other reddening laws (e.g., Calzetti et al. 2000) in UV region, particularly due to the presence/absence of UV bump at 2175 Å, which can alter the SED fitting results depending on the reddening law

used. Therefore, the UV region ( $< 4000$  Å) is excluded from our SED fitting.

For the SED fitting, an interactive data language (IDL) procedure, MPFIT (Markwardt 2009), is used. Figure 5 and 6 show examples of the best-fit SED models with the photometric data of unobscured and dust-obscured quasars, respectively. Through the SED fitting, we obtain the  $E(B - V)$  values and extinction-corrected  $L_{3,4}$  and  $L_{4,6}$  values, and these properties of the dust-

**Table 1.** Line and SED fitting results of dust-obscured quasars

object name	redshift	FWHM <sub>H<math>\beta</math></sub> <sup>†</sup> (km s <sup>-1</sup> )	FWHM <sub>H<math>\alpha</math></sub> <sup>†</sup> (km s <sup>-1</sup> )	log $L_{3.4}$ <sup>*</sup> (erg s <sup>-1</sup> )	log $L_{4.6}$ <sup>*</sup> (erg s <sup>-1</sup> )	$E(B - V)$ (mag.)
F2M0036–0113	0.294	–	2818±860	45.34±0.02	45.33±0.02	1.60±0.01
F2M0136–0052	0.718	6775±2109	–	45.37±0.02	45.36±0.02	0.48±0.01
F2M0729+3336	0.957	–	3182±970	46.16±0.03	46.15±0.03	0.50±0.01
F2M0810+4134	0.506	3815±1164	2989±912	44.71±0.03	44.69±0.03	0.21±0.01
F2M0817+4354	0.186	–	2901±903	44.59±0.02	44.57±0.02	0.80±0.01
F2M0830+3759	0.414	5923±1809	4562±1392	45.28±0.02	45.26±0.02	0.61±0.01
F2M0841+3604	0.553	–	2902±902	45.38±0.02	45.36±0.02	0.79±0.01
F2M0937+5008	0.275	2829±863	3527±1076	44.73±0.02	44.72±0.02	0.46±0.01
F2M1021+6311	0.138	–	3521±1074	44.52±0.02	44.50±0.02	0.65±0.01
F2M1038+6044	0.515	–	2804±855	45.81±0.02	45.79±0.02	0.87±0.01
F2M1040+5934	0.147	–	6468±1973	45.16±0.02	45.15±0.02	0.95±0.01
F2M1113+1244	0.681	3404±1038	–	46.36±0.02	46.35±0.02	0.90±0.01
F2M1117–0236	0.463	5983±1918	4523±1387	44.59±0.04	44.57±0.04	0.21±0.01
F2M1209–0107	0.363	–	2394±730	45.44±0.03	45.43±0.03	0.87±0.01
F2M1227+5053	0.768	3608±1101	–	45.86±0.03	45.85±0.03	0.33±0.01
F2M1227+3214	0.137	2822±861	2818±860	44.77±0.02	44.76±0.02	0.79±0.01
F2M1256–0200	0.835	2900±885	–	46.06±0.02	46.04±0.02	0.80±0.01
F2M1259+0729	0.860	–	2802±855	45.99±0.02	45.98±0.02	0.37±0.01
F2M1307+2338	0.275	–	2816±859	45.28±0.02	45.27±0.02	1.17±0.01
F2M1313+1453	0.584	–	3028±924	45.62±0.02	45.60±0.02	0.62±0.01
F2M1340+0514	0.264	–	2820±860	45.23±0.02	45.22±0.02	0.95±0.01
F2M1408+3243	0.338	–	3481±1062	44.21±0.04	44.20±0.04	0.42±0.01
F2M1415+3333	0.416	–	2854±870	45.31±0.02	45.29±0.02	0.61±0.01
F2M1434+0935	0.771	3819±1289	–	45.84±0.02	45.82±0.02	0.68±0.01
F2M1439+1555	0.941	–	4960±1513	45.36±0.04	45.34±0.04	0.23±0.02
F2M1517+2851	0.705	–	2798±853	45.95±0.02	45.93±0.02	0.64±0.01
F2M1605+0141	0.343	–	2796±853	45.58±0.02	45.56±0.02	1.02±0.01
F2M1642+3948	0.593	5383±1642	3878±1183	45.81±0.03	45.79±0.03	0.16±0.01
F2M1715+2807	0.523	–	3828±1168	45.64±0.02	45.62±0.02	0.91±0.01
F2M2325–1052	0.564	–	2083±635	45.11±0.03	45.10±0.03	0.38±0.01

**Notes.**
<sup>(†)</sup> The errors of FWHM<sub>H $\beta$</sub>  and FWHM<sub>H $\alpha$</sub>  are their FWHM<sub>tot, err</sub> values.

<sup>(\*)</sup> Dust extinction corrected luminosities.

obscured quasars are presented in Table 1. Moreover, since Kim et al. (2023) found that the measured  $L_{3.4}$  and  $L_{4.6}$  values based on the quasar spectrum of Krawczyk et al. (2013) are  $\sim 5\%$  higher than those from Assef et al. (2010), the discrepancy is added as an uncertainty in quadrature to their original uncertainties obtained from the fit. Furthermore, through the SED fitting, we can measure quasar fractions, defined as  $C_1 Q(\lambda)/f(\lambda)$ , at  $3.4\ \mu\text{m}$  and  $4.6\ \mu\text{m}$ . Since quasar activities of the dust-obscured and the unobscured quasars are dominant, we only use the SED fitting results for the sample with the measured quasar fractions exceeding 0.5.

### 3.3. $L_{\text{bol}}$ and $M_{\text{BH}}$ values

In this subsection, we estimate bolometric luminosities and black hole masses for both the dust-obscured and the unobscured quasars. However, given that dust-obscured quasars are heavily obscured, it is necessary to use  $L_{\text{bol}}$  and  $M_{\text{BH}}$  estimators that are immune to the dust extinction. Therefore, we use the  $L_{\text{MIR}}$ -based  $L_{\text{bol}}$  and  $M_{\text{BH}}$  estimators (Kim et al. 2023) that can measure these properties without the effects of the dust extinction.

For estimating the  $L_{\text{bol}}$  values, we use the extinction-corrected  $L_{4.6}$  values measured from the SED fitting with the

$L_{4.6}$ -based  $L_{\text{bol}}$  estimator (Kim et al. 2023). The used  $L_{4.6}$ -based  $L_{\text{bol}}$  estimator is

$$\log\left(\frac{L_{\text{bol}}}{10^{44}\ \text{erg s}^{-1}}\right) = (0.739 \pm 0.021) + (0.993 \pm 0.031) \log\left(\frac{L_{4.6}}{10^{44}\ \text{erg s}^{-1}}\right). \quad (2)$$

The measured  $L_{\text{bol}}$  values of the dust-obscured quasars are listed in Table 2.

To obtain the  $M_{\text{BH}}$  values, we use the  $L_{\text{MIR}}$ -based  $M_{\text{BH}}$  estimators (Kim et al. 2023), which are

$$\log\left(\frac{M_{\text{BH}}}{M_{\odot}}\right) = (6.914 \pm 0.023) + (0.478 \pm 0.016) \log\left(\frac{L_{4.6}}{10^{44}\ \text{erg s}^{-1}}\right) + 2 \log\left(\frac{\text{FWHM}_{\text{H}\beta}}{1000\ \text{km s}^{-1}}\right) \quad (3)$$

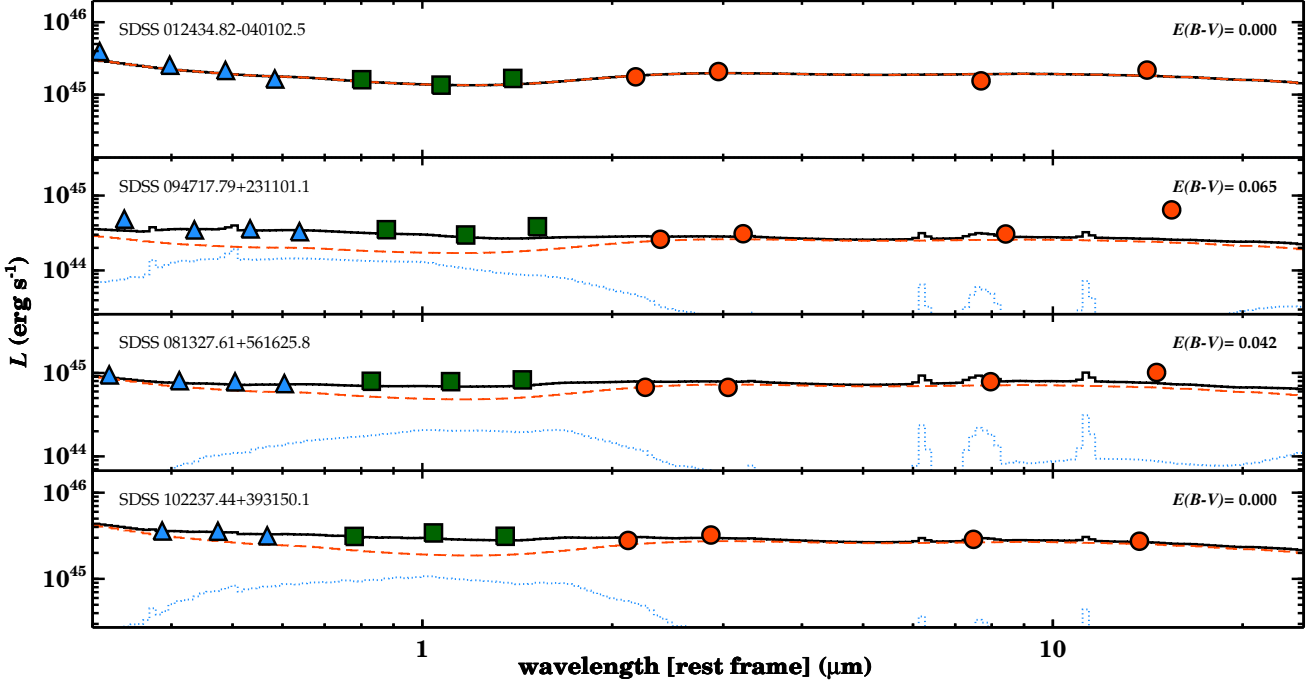


**Fig. 5.** Best-fit SED models and photometric data of four randomly selected unobscured quasars. Blue triangles, green squares, and red circles denote the photometric data points of SDSS, 2MASS PSC, and WISE, respectively. Red dashed and blue dotted lines mean the reddened spectra of quasar and host galaxy, respectively, and black solid lines represent the best-fit SED models. The name of the randomly selected sample and their  $E(B - V)$  values measured from the SED fitting are presented on the top-left and -right side of each panel, respectively.

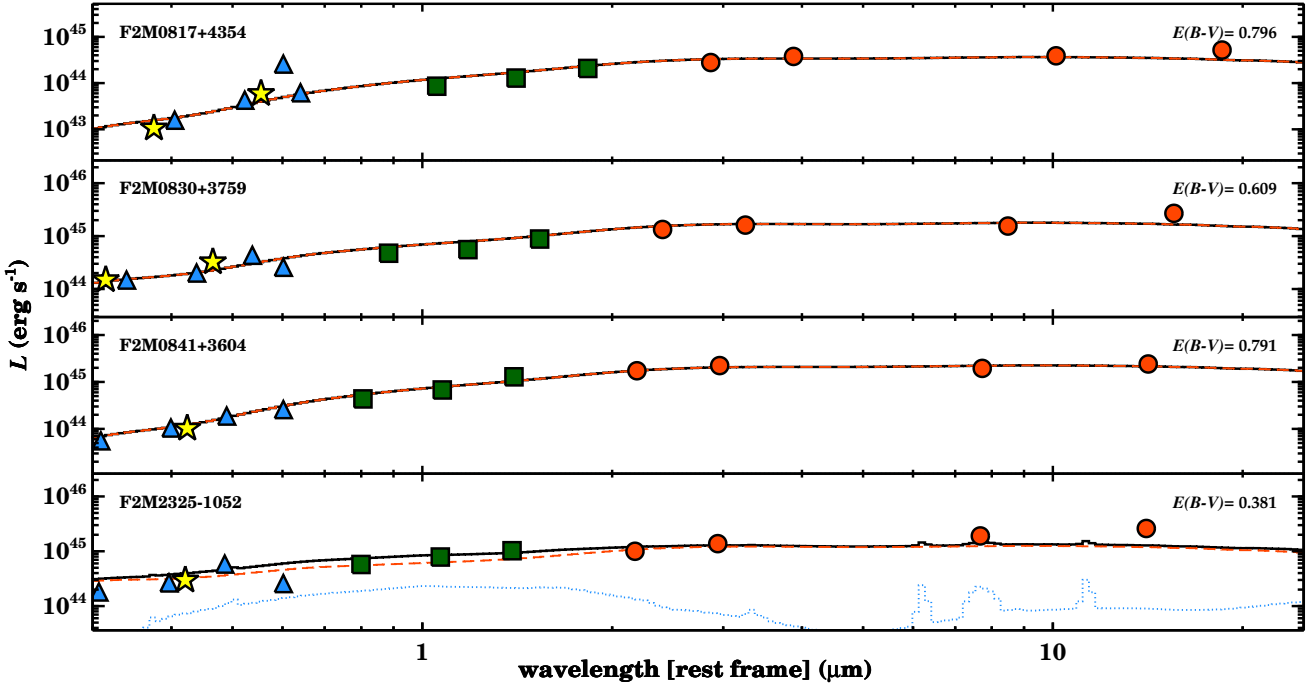


**Fig. 6.** Best-fit SED models and photometric data of four randomly selected dust-obscured quasars. The meanings of the symbols and lines are identical to those in Figure 5, but  $B$ - and  $R$ -band photometry are additionally shown as yellow stars.

and (4)

$$\log\left(\frac{M_{\text{BH}}}{M_{\odot}}\right) = (6.973 \pm 0.060) + (0.478 \pm 0.016) \log\left(\frac{L_{4.6}}{10^{44} \text{ erg s}^{-1}}\right) + (2.06 \pm 0.06) \log\left(\frac{\text{FWHM}_{\text{H}\alpha}}{1000 \text{ km s}^{-1}}\right).$$

For objects where both  $\text{FWHM}_{\text{H}\beta}$  and  $\text{FWHM}_{\text{H}\alpha}$  measurements are available, we use the  $M_{\text{BH}}$  values derived from  $\text{FWHM}_{\text{H}\alpha}$ . This is because, in the case of the dust-obscured quasars, some objects exhibit a broad component in the  $\text{H}\alpha$  line, while the broad component of the  $\text{H}\beta$  line is absent, suggesting that the



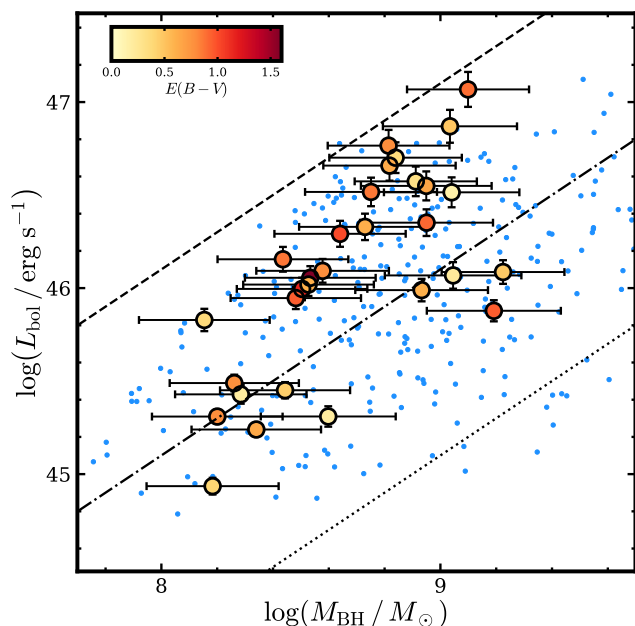


**Fig. 7.** Bolometric luminosities versus BH masses of dust-obscured and unobscured quasars. The dust-obscured quasars are open circles with the colors representing their  $E(B - V)$  values, and the unobscured quasars are blue dots. The dashed, dash-dotted, and dotted lines denote  $\lambda_{\text{Edd}}$  values of 1.0, 0.1, and 0.01, respectively.

$\text{FWHM}_{\text{H}\beta}$  could be affected by dust extinction in extreme cases. The measured  $M_{\text{BH}}$  values of the dust-obscured quasars are summarized in Table 2.

Similar to the dust-obscured quasars, we estimate the  $M_{\text{BH}}$  values of the unobscured quasars using Equations of 3 and 4. Among the 614 unobscured quasars selected in Section 2, 93 lack Balmer line measurements but exhibit Mg II line properties. We convert their  $\text{FWHM}_{\text{Mg II}}$  to  $\text{FWHM}_{\text{H}\beta}$  using the relationship presented in Bisogni et al. (2017), which are used to measure their  $M_{\text{BH}}$  values.

#### 4. Eddington Ratios

Using the  $L_{\text{bol}}$  and  $M_{\text{BH}}$  values, we measure  $\lambda_{\text{Edd}}$  ( $L_{\text{bol}}/L_{\text{Edd}}$ , where  $L_{\text{Edd}}$  is Eddington luminosity) values of the dust-obscured and unobscured quasars. The measured  $\lambda_{\text{Edd}}$  values of the dust-obscured quasars are also listed in Table 2.

A comparison of the  $L_{\text{bol}}$  and  $M_{\text{BH}}$  values of the dust-obscured and the unobscured quasars are shown in Figure 7, and Figure 8 shows distributions of the  $\lambda_{\text{Edd}}$  values. The median  $\log(\lambda_{\text{Edd}})$  values of the dust-obscured and the unobscured quasars are  $-0.61 \pm 0.38$  and  $-0.98 \pm 0.49$ , respectively, which shows that the  $\lambda_{\text{Edd}}$  values of the dust-obscured quasars are significantly higher than those of the unobscured quasars. In order to quantify how these  $\lambda_{\text{Edd}}$  values are significantly different, we perform a Kolmogorov-Smirnov test (K-S test) using SciPy package (Virtanen et al. 2020) on Python. The maximum deviation between the cumulative distribution of these two  $\lambda_{\text{Edd}}$  values,  $D$ , is 0.36, and the probability of the result given the null hypothesis,  $p$ , is 0.001, indicating that they have different distributions.

Since  $\lambda_{\text{Edd}}$  values can vary with redshift due to sample bias effects or cosmological evolution, we compare the  $\lambda_{\text{Edd}}$  values

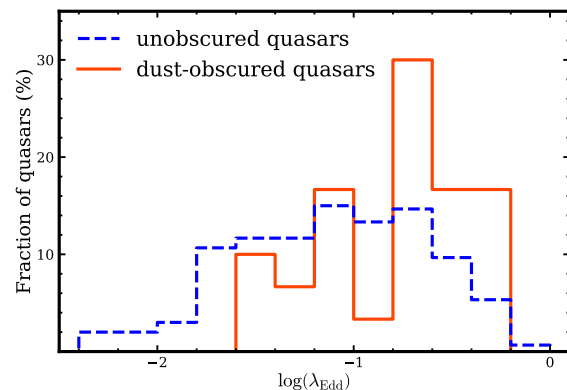


**Fig. 8.** Distribution of  $\lambda_{\text{Edd}}$  values of dust-obscured and unobscured quasars. Red solid and blue dashed histograms mean the dust-obscured and the unobscured quasars, respectively.

of the two kinds of quasars across their redshifts. The comparison is shown in Figure 9. For the comparison, we divide the two kinds of quasars into six bins of redshift:  $0.10 \sim 0.25$ ,  $0.25 \sim 0.40$ ,  $0.40 \sim 0.55$ ,  $0.55 \sim 0.70$ ,  $0.70 \sim 0.85$ , and  $0.85 \sim 1.00$ . The  $\log(\lambda_{\text{Edd}})$  values of the dust-obscured quasars in the six redshift bins are  $-1.10 \pm 0.21$ ,  $-0.61 \pm 0.33$ ,  $-0.83 \pm 0.34$ ,  $-0.50 \pm 0.18$ ,  $-0.44 \pm 0.38$ , and  $-0.26 \pm 0.39$ , and those of the unobscured quasars are  $-1.30 \pm 0.45$ ,  $-1.27 \pm 0.42$ ,  $-1.07 \pm 0.49$ ,  $-0.75 \pm 0.38$ ,  $-0.67 \pm 0.41$ , and  $-0.82 \pm 0.44$ . This comparison reveals that the  $\lambda_{\text{Edd}}$  values of the dust-obscured quasars are significantly higher than those of the unobscured quasars for a wide redshift range ( $0 \lesssim z \lesssim 1$ ).

Furthermore, given that  $\lambda_{\text{Edd}}$  can be affected by BH mass (e.g., Shen et al. 2011; Kim et al. 2015a), we also compare the  $\lambda_{\text{Edd}}$  distributions of four sub-samples divided by BH mass and redshift to mitigate the effects of BH mass and redshift on the  $\lambda_{\text{Edd}}$  distribution. First, we divide the dust-obscured quasars and the unobscured quasars into low- $z$  ( $0.137 \leq z \leq 0.5$ ) and high- $z$  ( $0.5 < z \leq 0.957$ ) samples. For the low- $z$  sample, we divide them into low- $z$  and low-mass ( $10^{8.15} M_{\odot} \leq M_{\text{BH}} \leq 10^{8.50} M_{\odot}$ ) and low- $z$  and high-mass ( $10^{8.50} M_{\odot} < M_{\text{BH}} \leq 10^{9.22} M_{\odot}$ ) sub-samples. For the low- $z$  and low-mass sub-sample, 7 dust-obscured quasars and 32 unobscured quasars are selected, and their  $\log(\lambda_{\text{Edd}})$  values are  $-0.99 \pm 0.31$  and  $-0.94 \pm 0.36$ , respectively. The  $\lambda_{\text{Edd}}$  values of the dust-obscured and unobscured quasars are similar, with a considerable overlap due to large uncertainties. However, in other sub-samples, more significant differences are found. For the low- $z$  and high-mass sub-sample, 7 dust-obscured quasars and 74 unobscured quasars are selected, and their  $\log(\lambda_{\text{Edd}})$  values are  $-0.61 \pm 0.38$  and  $-1.33 \pm 0.35$ , respectively. After that, for the high- $z$  sample, we also divide them into high- $z$  and low-mass ( $10^{8.15} M_{\odot} \leq M_{\text{BH}} \leq 10^{8.90} M_{\odot}$ ) and high- $z$  and high-mass ( $10^{8.90} M_{\odot} < M_{\text{BH}} \leq 10^{9.22} M_{\odot}$ ) sub-samples. For the high- $z$  and low-mass sub-sample, 8 dust-obscured quasars and 65 unobscured quasars are chosen, and their  $\log(\lambda_{\text{Edd}})$  values are  $-0.38 \pm 0.24$  and  $-0.52 \pm 0.31$ , respectively. Moreover, for the high- $z$  and high-mass sub-sample, we obtain 8 dust-obscured quasars and 43 unobscured quasars, and their  $\log(\lambda_{\text{Edd}})$  values are  $-0.56 \pm 0.36$  and  $-0.82 \pm 0.28$ , respectively. Overall, the  $\lambda_{\text{Edd}}$  of the dust-obscured quasars are significantly higher than those of the unobscured quasars in the limited redshift and  $M_{\text{BH}}$  range, and these comparisons are shown in Figure 10.

**Table 2.** BH properties of dust-obscured quasars

object name	$\log(L_{\text{bol}}/\text{erg s}^{-1})$	$\log(M_{\text{BH}}/M_{\odot})$	$\log(\lambda_{\text{Edd}})$
F2M0036–0113	46.06±0.06	8.53±0.23	−0.58±0.24
F2M0136–0052	46.09±0.06	9.22±0.22	−1.24±0.22
F2M0729+3336	46.87±0.09	9.03±0.24	−0.26±0.25
F2M0810+4134	45.43±0.05	8.28±0.24	−0.96±0.24
F2M0817+4354	45.31±0.04	8.20±0.23	−0.99±0.24
F2M0830+3759	45.99±0.06	8.93±0.24	−1.04±0.24
F2M0841+3604	46.09±0.06	8.58±0.24	−0.59±0.24
F2M0937+5008	45.45±0.04	8.44±0.23	−1.09±0.24
F2M1021+6311	45.24±0.04	8.34±0.23	−1.20±0.23
F2M1038+6044	46.52±0.08	8.75±0.24	−0.33±0.24
F2M1040+5934	45.88±0.06	9.19±0.24	−1.41±0.24
F2M1113+1244	47.07±0.09	9.10±0.22	−0.13±0.23
F2M1117–0236	45.31±0.05	8.60±0.24	−1.39±0.24
F2M1209–0107	46.15±0.07	8.44±0.23	−0.38±0.24
F2M1227+5053	46.57±0.08	8.91±0.22	−0.44±0.23
F2M1227+3214	45.49±0.04	8.26±0.23	−0.87±0.23
F2M1256–0200	46.77±0.08	8.81±0.22	−0.15±0.23
F2M1259+0729	46.70±0.08	8.84±0.24	−0.24±0.24
F2M1307+2338	46.00±0.06	8.50±0.23	−0.61±0.24
F2M1313+1453	46.33±0.07	8.73±0.24	−0.50±0.24
F2M1340+0514	45.95±0.06	8.48±0.23	−0.64±0.24
F2M1408+3243	44.94±0.04	8.18±0.24	−1.35±0.24
F2M1415+3333	46.02±0.06	8.53±0.23	−0.61±0.24
F2M1434+0935	46.55±0.08	8.95±0.23	−0.50±0.24
F2M1439+1555	46.07±0.07	9.05±0.24	−1.08±0.25
F2M1517+2851	46.66±0.08	8.82±0.24	−0.26±0.24
F2M1605+0141	46.29±0.07	8.64±0.24	−0.45±0.24
F2M1642+3948	46.51±0.08	9.04±0.24	−0.63±0.25
F2M1715+2807	46.35±0.07	8.95±0.24	−0.70±0.24
F2M2325–1052	45.83±0.06	8.15±0.23	−0.43±0.24

## 5. Discussion

### 5.1. Comparisons of $L_{\text{bol}}$ and $M_{\text{BH}}$ Values of Dust-obscured Quasars from Different Estimators

The  $L_{\text{bol}}$  and  $M_{\text{BH}}$  values of dust-obscured quasars have been measured using various methods (Kim & Im 2018; Urrutia et al. 2012). In this subsection, we examine the consistency between the  $L_{\text{bol}}$  and  $M_{\text{BH}}$  values measured with the  $L_{\text{MIR}}$ -based estimators and those obtained from the different methods used in Kim & Im (2018) and Urrutia et al. (2012).

Nine and four of our dust-obscured quasars are overlapped with the dust-obscured quasars studied in Kim & Im (2018) and Urrutia et al. (2012), respectively. Using these objects, we compare the  $L_{\text{bol}}$  and  $M_{\text{BH}}$  values from our method versus those from other methods. First, for the nine dust-obscured quasars, we compare their  $L_{\text{bol}}$  and  $M_{\text{BH}}$  values from the  $L_{\text{MIR}}$ -based estimators to those from Paschen line-based estimators (Kim et al. 2010, 2022). Kim & Im (2018) measured their  $P\beta$  or  $P\alpha$  line properties, luminosity and FWHM, and their  $L_{\text{bol}}$  and  $M_{\text{BH}}$  values can be measured with the Paschen line-based estimators established in Kim et al. (2022) and Kim et al. (2010), respectively. The Paschen line-based  $L_{\text{bol}}$  estimators (Kim et al. 2022) are

$$\log\left(\frac{L_{\text{bol}}}{10^{42} \text{ erg s}^{-1}}\right) = (1.31 \pm 0.09) + (0.97 \pm 0.05) \log\left(\frac{L_{P\beta}}{10^{40} \text{ erg s}^{-1}}\right) \quad (5)$$

and

$$\log\left(\frac{L_{\text{bol}}}{10^{42} \text{ erg s}^{-1}}\right) = (1.43 \pm 0.11) + (0.87 \pm 0.06) \log\left(\frac{L_{P\alpha}}{10^{40} \text{ erg s}^{-1}}\right). \quad (6)$$

Moreover, the Paschen line-based  $M_{\text{BH}}$  estimators (Kim et al. 2010) are

$$\log\left(\frac{M_{\text{BH}}}{M_{\odot}}\right) = (7.33 \pm 0.10) + (0.45 \pm 0.03) \log\left(\frac{L_{P\beta}}{10^{42} \text{ erg s}^{-1}}\right) + (1.69 \pm 0.16) \log\left(\frac{\text{FWHM}_{P\beta}}{10^3 \text{ km s}^{-1}}\right) \quad (7)$$

and

$$\log\left(\frac{M_{\text{BH}}}{M_{\odot}}\right) = (7.29 \pm 0.10) + (0.43 \pm 0.03) \log\left(\frac{L_{P\alpha}}{10^{42} \text{ erg s}^{-1}}\right) + (1.92 \pm 0.18) \log\left(\frac{\text{FWHM}_{P\alpha}}{10^3 \text{ km s}^{-1}}\right). \quad (8)$$

Note that the FWHM and luminosity of both the  $P\beta$  and  $P\alpha$  lines for 1307+2338 were measured in Kim & Im (2018), and its  $L_{\text{bol}}$  and  $M_{\text{BH}}$  values from both lines are used in this comparison.

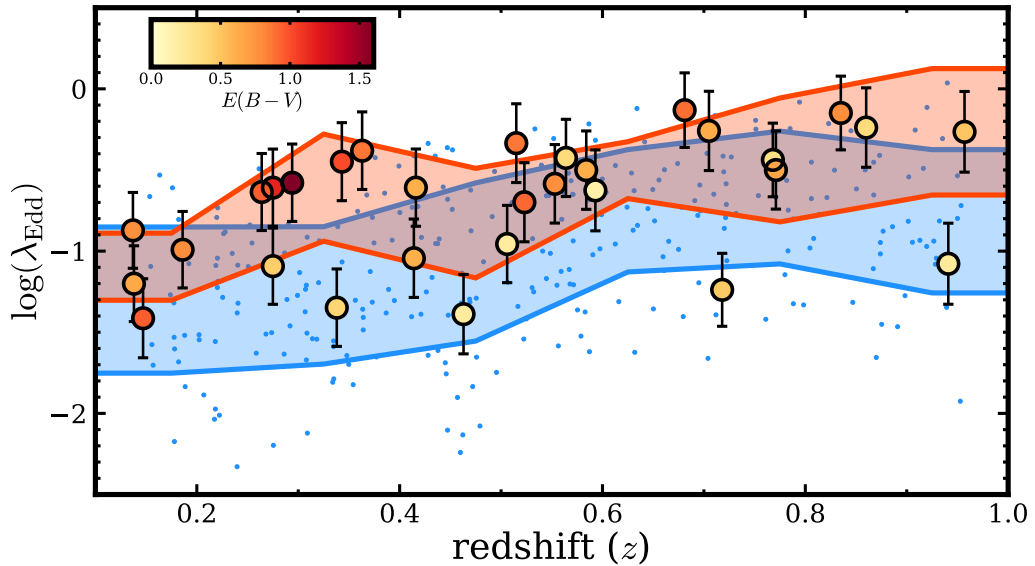


**Fig. 9.**  $\log \lambda_{\text{Edd}}$  values vs. redshifts. The meanings of open circles and blue dots are identical to Figure 7. Red and blue polygons represent the  $\log \lambda_{\text{Edd}}$  values and their standard deviations of dust-obscured and unobscured quasars, respectively, which are divided into six sub-samples by redshifts.

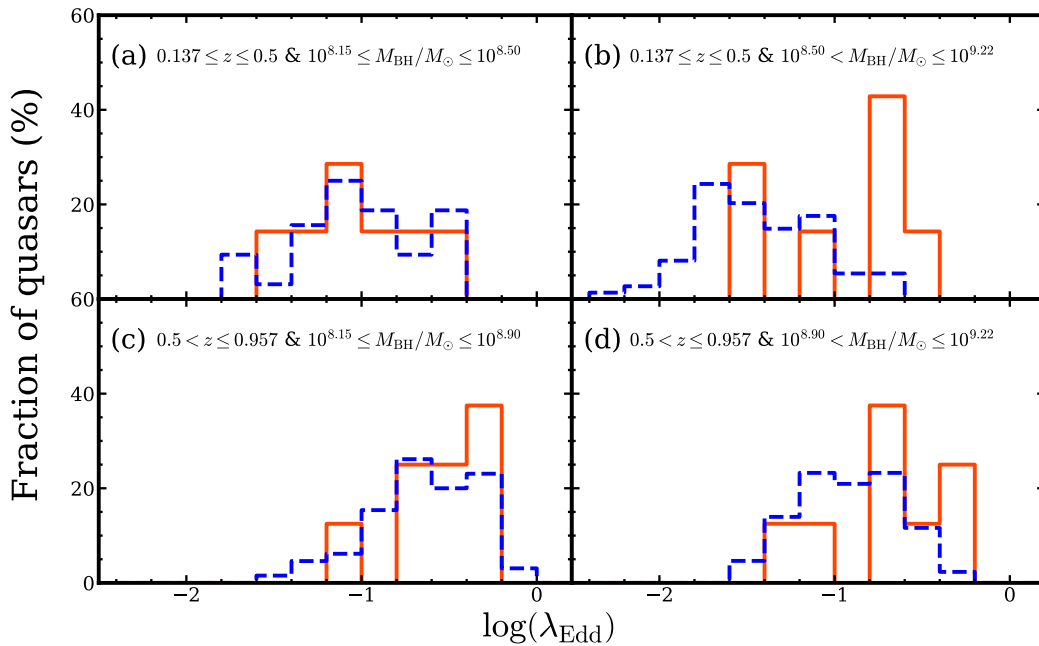


**Fig. 10.** (a)  $\lambda_{\text{Edd}}$  distributions for low- $z$  and low-mass quasars. Red solid and blue dashed histograms denote the dust-obscured and the unobscured quasars, respectively. (b)  $\lambda_{\text{Edd}}$  distributions for low- $z$  and high-mass quasars. (c)  $\lambda_{\text{Edd}}$  distributions for high- $z$  and low-mass quasars. (d)  $\lambda_{\text{Edd}}$  distributions for high- $z$  and high-mass quasars.

The measured  $L_{\text{bol}}$  and  $M_{\text{BH}}$  values based on the Paschen lines are summarized in Table 3.

Second, Urrutia et al. (2012) measured the monochromatic luminosities,  $\lambda L_{\lambda}$ , at  $15 \mu\text{m}$  (hereafter,  $L_{15}$ ) and FWHM values of Balmer lines for the four dust-obscured quasars. Their  $L_{15}$  values can be converted to the  $L_{4.6}$  values by applying the ratio of  $L_{15}$  to  $L_{4.6}$  in the quasar template of Krawczyk et al. (2013), and the  $L_{\text{bol}}$  values can be measured with Equation 2 using the converted  $L_{4.6}$  values. Additionally, the  $M_{\text{BH}}$  values can be measured with Equations 3 and 4 after converting the  $L_{15}$  values to  $L_{4.6}$  values

using the ratio. The measured  $L_{\text{bol}}$  and  $M_{\text{BH}}$  values from the  $L_{15}$  are listed in Table 3.

Figure 11 (a) presents a comparison of the  $L_{\text{bol}}$  values, showing a reasonable agreement between the two independent estimations, and their Pearson correlation coefficient is 0.831. Overall, the  $L_{\text{bol}}$  values derived in this work are slightly overestimated compared to the  $L_{\text{bol}}$  values obtained through the different methods, yet there is no clear tendency.

Furthermore, a comparison of the  $M_{\text{BH}}$  values is also presented in Figure 11 (b). Compared to the  $L_{\text{bol}}$  comparison, there is a far less substantial agreement between the  $M_{\text{BH}}$  values, and

**Table 3.** BH properties of dust-obscured quasars from different estimators

object name	$\log(L_{\text{bol}}/\text{erg s}^{-1})$			$\log(M_{\text{BH}}/M_{\odot})$		
	P $\beta$	P $\alpha$	$L_{15}^a$	P $\beta$	P $\alpha$	$L_{15}$
F2M0036–0113	45.46±0.22	–	–	7.85±0.19	–	–
F2M0729+3336	–	–	46.55	–	–	8.70±0.13 <sup>b</sup>
F2M0817+4354	–	45.14±0.23	–	–	8.24±0.28	–
F2M0830+3759	–	–	46.05	–	–	8.69±0.11 <sup>b</sup>
F2M0841+3604	–	–	45.95	–	–	8.65±0.26 <sup>c</sup>
F2M1113+1244	46.49±0.28	–	46.84	8.43±0.24	–	8.64±0.18 <sup>b</sup>
F2M1209–0107	46.21±0.26	–	–	8.87±0.29	–	–
F2M1227+5053	46.20±0.32	–	–	8.52±0.36	–	–
F2M1307+2338	45.24±0.21	45.53±0.25	–	7.79±0.20	8.06±0.24	–
F2M1313+1453	46.30±0.25	–	–	8.79±0.25	–	–
F2M1434+0935	46.21±0.25	–	–	8.02±0.18	–	–
F2M2325–1052	46.12±0.37	–	–	8.48±0.46	–	–

**Notes.**

<sup>(a)</sup> The uncertainty for  $L_{15}$  is not provided by Urrutia et al. (2012). The uncertainty for  $L_{\text{bol}}$  presented in Figure 11 is estimated on an assumption that  $L_{15}$ 's uncertainty amounts to 10 % of its value.

<sup>(b)</sup> The  $M_{\text{BH}}$  values are measured based on  $L_{15}$  values and H $\beta$  widths.

<sup>(c)</sup> The  $M_{\text{BH}}$  values are measured based on  $L_{15}$  values and H $\alpha$  widths.

their Pearson correlation coefficient is only 0.257. This weak agreement might be due to their limited  $M_{\text{BH}}$  range, but the impact of the less robust line widths between Paschen and Balmer lines (e.g., Landt et al. 2013) as a contributing factor cannot be ruled out.

### 5.2. Validity of $L_{\text{MIR}}$ -based $L_{\text{bol}}$ estimators up to $z = 2.5$

In this subsection, we explore the applicability of the  $L_{\text{MIR}}$  estimators up to  $z = 2.5$ , which were established using only SDSS quasars at  $z \lesssim 0.5$  (Kim et al. 2023). To determine whether there is any significant deviation between the  $L_{\text{MIR}}$ -based  $L_{\text{bol}}$  values and those derived from other estimators up to  $z = 2.5$ , we compare the  $L_{\text{bol}}$  values from the  $L_{4,6}$ -based estimator to those measured from UV- and optical-based estimators (Kim et al. 2023; Runnoe et al. 2012) that were established with continuum luminosities,  $\lambda L_{\lambda}$ , at 3000 Å and 5100 Å (hereafter, L3000 and L5100, respectively).

For the comparison, we select 1046 SDSS quasars at  $z < 2.5$  among the SDSS DR14 quasars (Pâris et al. 2018), following the selection method for unobscured quasars described in Section 2. Rakshit et al. (2020) measured the L3000 and L5100 values for 959 and 563 SDSS quasars, respectively. Their  $L_{\text{bol}}$  values can be estimated with the L3000- and L5100-based  $L_{\text{bol}}$  estimators. The L3000-based  $L_{\text{bol}}$  estimator (Runnoe et al. 2012) is

$$\log\left(\frac{L_{\text{bol}}}{10^{44} \text{ erg s}^{-1}}\right) = (0.53 \pm 1.27) + (0.97 \pm 0.03) \log\left(\frac{\text{L3000}}{10^{44} \text{ erg s}^{-1}}\right), \quad (9)$$

and the L5100-based  $L_{\text{bol}}$  estimator (Kim et al. 2023) is

$$\log\left(\frac{L_{\text{bol}}}{10^{44} \text{ erg s}^{-1}}\right) = (0.764 \pm 0.019) + (0.978 \pm 0.029) \log\left(\frac{\text{L5100}}{10^{44} \text{ erg s}^{-1}}\right). \quad (10)$$

Figure 12 (a) shows the comparison of  $L_{\text{bol}}$  derived from  $L_{4,6}$  with those from L3000 and L5100, exhibiting a Pearson correlation coefficient of 0.952. Moreover, we investigate whether there is a redshift dependence for the  $L_{\text{bol}}$  values measured from  $L_{4,6}$  compared to those from other methods, as shown in Figure 13. However, we found no evidence of redshift dependence. Thus, although the  $L_{4,6}$ -based  $L_{\text{bol}}$  estimator was established using the SDSS quasars at  $z \lesssim 0.5$ , our results demonstrate that the  $L_{4,6}$ -based estimator accurately measures  $L_{\text{bol}}$  for quasars up to  $z = 2.5$ .

Additionally, we compare  $M_{\text{BH}}$  derived from  $L_{4,6}$  to those measured from other estimators. Among the 1046 SDSS quasars at  $z < 2.5$ , Rakshit et al. (2020) measured  $M_{\text{BH}}$  values for 190 and 557 SDSS quasars using the L5100 combined with FWHM $_{\text{H}\alpha}$  and FWHM $_{\text{H}\beta}$ , respectively. Furthermore, Rakshit et al. (2020) also estimated  $M_{\text{BH}}$  values for 804 SDSS quasars using L3000 and FWHM $_{\text{Mg II}}$ . For the comparison, we determine  $M_{\text{BH}}$  values based on  $L_{4,6}$  using Equation 3 or 4 for objects with measurements of FWHM $_{\text{H}\beta}$  or FWHM $_{\text{H}\alpha}$ , respectively. For objects with FWHM $_{\text{Mg II}}$  measurements, we estimate their  $M_{\text{BH}}$  values using Equation 3 after converting FWHM $_{\text{Mg II}}$  to FWHM $_{\text{H}\beta}$ , based on the relationship described by Bisogni et al. (2017). Figure 12 (b) presents the comparison of  $M_{\text{BH}}$  derived from  $L_{4,6}$  against those from L3000 and L5100, demonstrating the reliability of the  $L_{4,6}$ -based  $M_{\text{BH}}$  estimators up to  $z = 2.5$ . The Pearson correlation coefficient between the two quantities is 0.984. Note that in this comparison, we use the FWHM values measured from the same line, thus not accounting for the relationships and distributions between FWHM values of different lines (e.g., Kim et al. 2010; Landt et al. 2013; Bisogni et al. 2017).

Although only some dust-obscured quasars at high- $z$  have been found to date (e.g., Banerji et al. 2015), it is expected that a significant number of high- $z$  dust-obscured quasars will be discovered through future IR surveys, such as Spectro-Photometer for the History of the Universe, Epoch of Reionization, and Ices Explorer (SPHEREx; Doré et al. 2014). As a result, the  $L_{\text{MIR}}$ -based estimators are expected to play an important role for

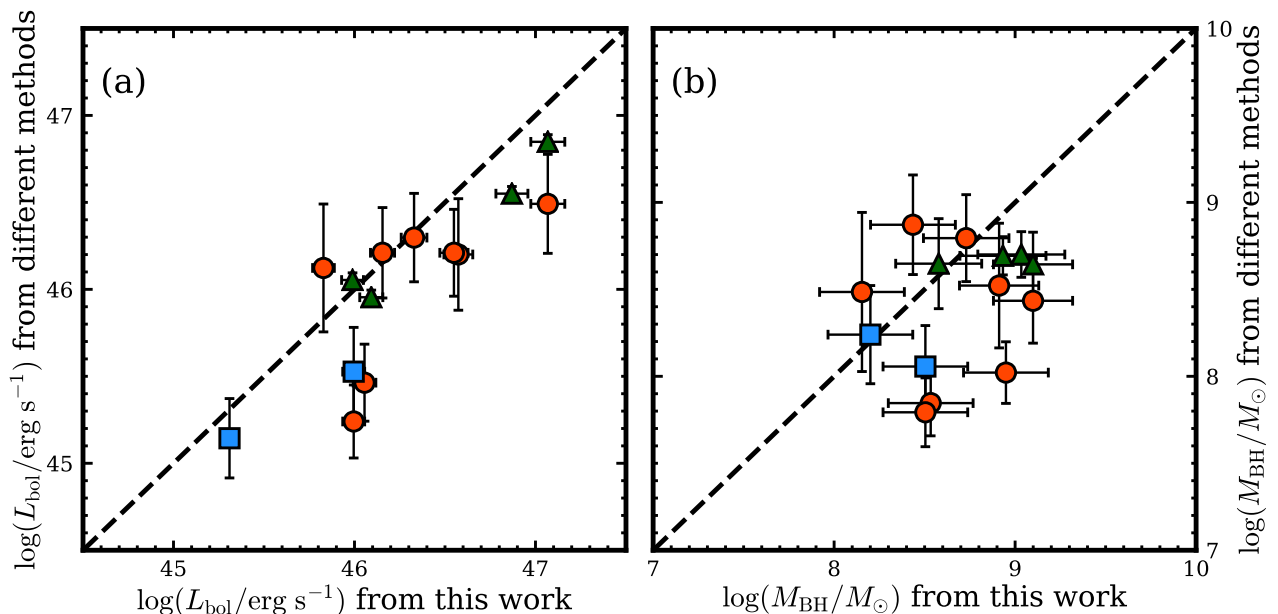


**Fig. 11.** (a) Comparison of  $L_{\text{bol}}$  values from this work and different estimators. Red circles, blue squares, and green triangles denote the  $L_{\text{bol}}$  values are derived by using  $P\beta$ ,  $P\alpha$ , and  $L_{15}$ , respectively. The dashed line denotes a line where the  $L_{\text{bol}}$  values are identical. (b)  $M_{\text{BH}}$  values from this work versus those from different methods. Red circles and blue squares represent that the  $M_{\text{BH}}$  values are measured with  $P\beta$  and  $P\alpha$  lines, respectively. Green triangles denote the  $M_{\text{BH}}$  values are estimated from  $L_{15}$  and Balmer line width. The dashed line represents a line where the  $M_{\text{BH}}$  values are identical.

unveiling the intrinsic properties of these high- $z$  dust-obscured quasars.

## 6. Conclusions

In the merger-driven galaxy evolution scenario as presented in Figure 1, dust-obscured quasars are expected to occur as the intermediate stage galaxies between ULIRGs and unobscured quasars. This scenario is supported by the higher  $\lambda_{\text{Edd}}$  values of dust-obscured quasars compared to those of unobscured quasars (Kim et al. 2015a; Kim & Im 2018). Although the BH activities of dust-obscured quasars are obscured, the previous studies used IR spectroscopic data to minimize the effects of dust extinction. However, the previous studies used the limited number of samples owing to (i) considerable expense associated with obtaining the IR spectroscopic data; (ii) the limited IR wavelength window in the atmosphere. As a result, only a limited number of dust-obscured quasars have been studied, yielding statistics that are not robust and confined to narrow redshift ranges.

In order to overcome these limitations of the previous studies, we estimated the  $\lambda_{\text{Edd}}$  values of 30 dust-obscured quasars at  $z \lesssim 1$  using the  $L_{4.6}$ -based  $L_{\text{bol}}$  and  $M_{\text{BH}}$  estimators (Kim et al. 2023) that have the advantages of being widely applicable. Compared to the control sample of unobscured quasars, we found that the  $\lambda_{\text{Edd}}$  values of the dust-obscured quasars are significantly higher than those of the unobscured ones. This result was consistent across the wide redshift range ( $z \lesssim 1$ ), and identical outcomes were yielded even when the analysis was constrained by  $M_{\text{BH}}$  or redshift.

Including our results, several observational studies have found that dust-obscured quasars have (i) high  $\lambda_{\text{Edd}}$  values (Urrutia et al. 2012; Kim et al. 2015a, 2018), (ii) high fractions of merging features in their host galaxies (Urrutia et al. 2008;

Glikman et al. 2015), (iii) dusty red colors (Kim & Im 2018), (iv) merging SMBH systems (Kim et al. 2020), and (v) enhanced star-formation activities (Georgakakis et al. 2009). These findings strongly support the picture that dust-obscured quasars are the intermediate stage galaxies between ULIRGs and unobscured quasars, as outlined in Figure 1.

*Acknowledgements.* D.K. acknowledges the support of the National Research Foundation of Korea (NRF) grant (Nos. 2021R1C1C1013580 and 2022R1A4A3031306) funded by the Korean Government (MSIT). Y. K. was supported by the National Research Foundation of Korea (NRF) grant funded by the Korean government (MSIT) (No. 2021R1C1C2091550). M.I. acknowledge the support from the National Research Foundation of Korea (NRF) grants, No. 2020R1A2C3011091, and No. 2021M3F7A1084525, funded by the Korea government (MSIT). M.K. acknowledges the support by the National Research Foundation of Korea (NRF) grant (No. 2022R1A4A3031306). G.L. acknowledges support from the Basic Science Research Program through NRF funded by MSIT (No.2022R1A6A3A01085930).

## References

- Alexander, D. M. & Hickox, R. C. 2012, *New A Rev.*, 56, 93
- Ananna, T. T., Urry, C. M., Ricci, C., et al. 2022, *ApJ*, 939, L13
- Ananna, T. T., Weigel, A. K., Trakhtenbrot, B., et al. 2022, *ApJS*, 261, 9
- Anderson, S. F., Voges, W., Margon, B., et al. 2003, *AJ*, 126, 2209
- Antonucci, R. 1993, *ARA&A*, 31, 473
- Assef, R. J., Kochanek, C. S., Brodwin, M., et al. 2010, *ApJ*, 713, 970
- Banerji, M., Alaghband-Zadeh, S., Hewett, P. C., et al. 2015, *MNRAS*, 447, 3368
- Becker, R. H., White, R. L., & Helfand, D. J. 1995, *ApJ*, 450, 559
- Becker, R. H., White, R. L., Gregg, M. D., et al. 2001, *ApJS*, 135, 227
- Bisogni, S., di Serego Alighieri, S., Goldoni, P., et al. 2017, *A&A*, 603, A1
- Boroson, T. A. 2002, *ApJ*, 565, 78
- Calistro Rivera, G., Alexander, D. M., Rosario, D. J., et al. 2021, *A&A*, 649, A102
- Calzetti, D., Armus, L., Bohlin, R. C., et al. 2000, *ApJ*, 533, 682
- Comastri, A., Fiore, F., Vignali, C., et al. 2001, *MNRAS*, 327, 781
- Croom, S. M., Smith, R. J., Boyle, B. J., et al. 2004, *MNRAS*, 349, 1397
- Cutri, R. M., Nelson, B. O., Kirkpatrick, J. D., Huchra, J. P., & Smith, P. S. 2001, *The New Era of Wide Field Astronomy*, 232, 78

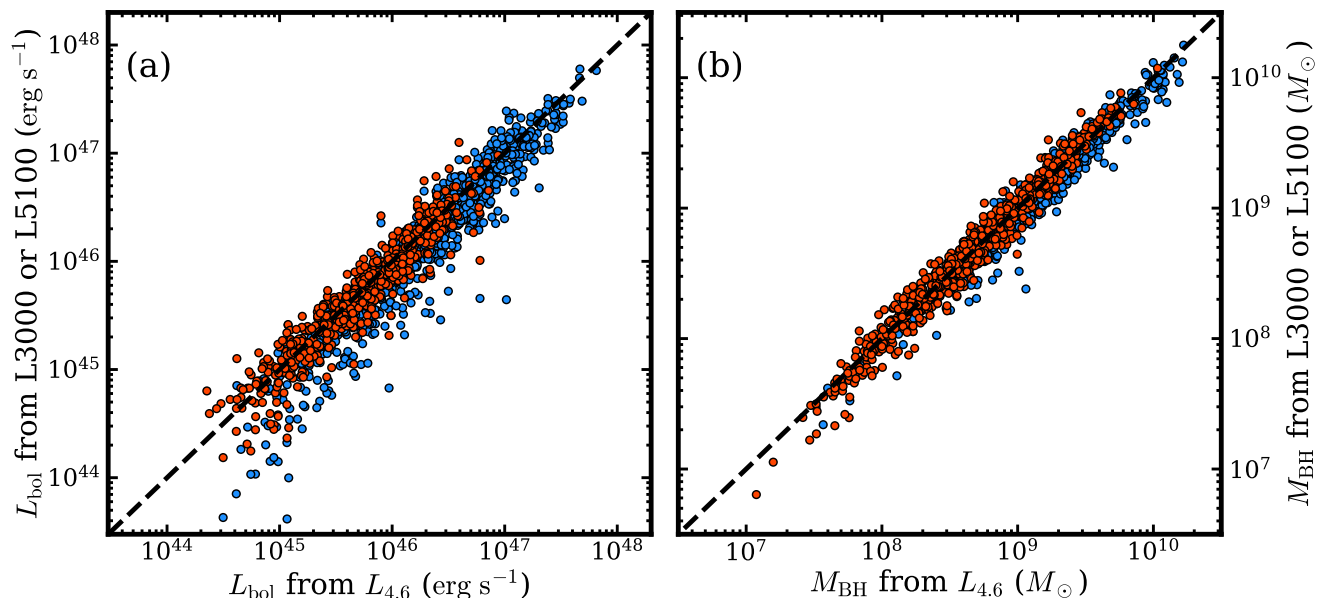


**Fig. 12.** (a) Comparison of  $L_{\text{bol}}$  values from  $L_{4.6}$  and those obtained using different estimators. Red circles mean the  $L_{\text{bol}}$  values derived from L5100, while blue circles denote those derived from L3000. The dashed line is a line where the  $L_{\text{bol}}$  values are identical. (b)  $M_{\text{BH}}$  values measured based on  $L_{4.6}$  versus those from different methods. Red circles represent the comparison of  $M_{\text{BH}}$  values measured using  $L_{4.6}$  and  $\text{FWHM}_{\text{H}}$ , compared to those derived from L5100 and  $\text{FWHM}_{\text{H}}$ . Meanwhile, blue circles denote the  $M_{\text{BH}}$  values derived using  $L_{4.6}$  and  $\text{FWHM}_{\text{Mg II}}$ , versus those from L3000 and  $\text{FWHM}_{\text{Mg II}}$ . The dashed line denotes a line where the  $M_{\text{BH}}$  values are identical.

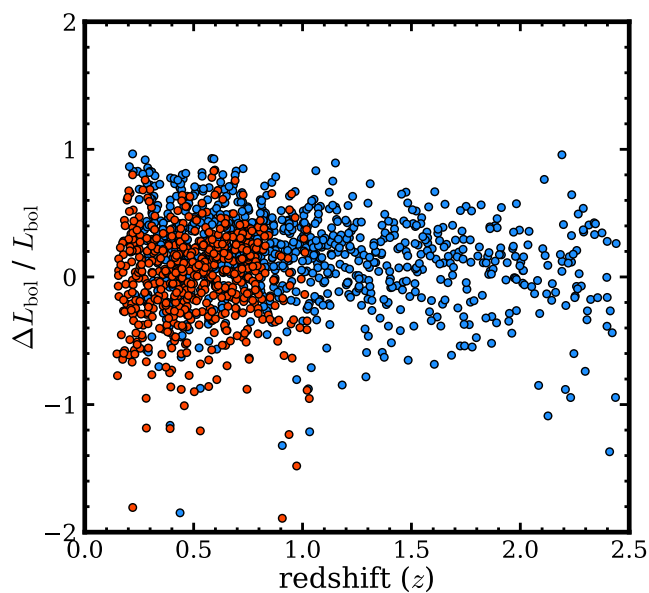


**Fig. 13.** Redshift versus  $\Delta L_{\text{bol}}/L_{\text{bol}}$ , where  $\Delta L_{\text{bol}}$  means the discrepancy between  $L_{\text{bol}}$  measured from  $L_{4.6}$  and that from either L3000 or L5100. Red and blue circles denote that the  $L_{\text{bol}}$  values are derived from L5100 and L3000, respectively.

Cutri, R. M., Nelson, B. O., Francis, P. J., & Smith, P. S. 2002, IAU Colloq. 184: AGN Surveys, 284, 127  
 Cutri, R. M., Skrutskie, M. F., van Dyk, S., et al. 2003, “The IRSA 2MASS All-Sky Point Source Catalog, NASA/IPAC Infrared Science Archive”  
 Di Matteo, T., Springel, V., & Hernquist, L. 2005, Nature, 433, 604

Dong, X., Wang, T., Wang, J., et al. 2008, MNRAS, 383, 581  
 Doré, O., Bock, J., Ashby, M., et al. 2014, arXiv:1412.4872  
 Ferrarese, L., & Merritt, D. 2000, ApJ, 539, L9  
 Fitzpatrick, E. L. 1999, PASP, 111, 63  
 Gebhardt, K., Bender, R., Bower, G., et al. 2000, ApJ, 539, L13  
 Georgakakis, A., Clements, D. L., Bendo, G., et al. 2009, MNRAS, 394, 533  
 Georgantopoulos, I., Pouliaxis, E., Mountrichas, G., et al. 2023, A&A, 673, A67  
 Glikman, E., Gregg, M. D., Lacy, M., et al. 2004, ApJ, 607, 60  
 Glikman, E., Helfand, D. J., White, R. L., et al. 2007, ApJ, 667, 673  
 Glikman, E., Urrutia, T., Lacy, M., et al. 2012, ApJ, 757, 51  
 Glikman, E., Simmons, B., Maily, M., et al. 2015, ApJ, 806, 218  
 Glikman, E., LaMassa, S., Piconcelli, E., et al. 2024, MNRAS, 528, 711  
 Grazian, A., Cristiani, S., D’Odorico, V., Omizzolo, A., & Pizzella, A. 2000, AJ, 119, 2540  
 Greene, J. E., & Ho, L. C. 2005, ApJ, 630, 122  
 Guo, H., Liu, X., Shen, Y., et al. 2019, MNRAS, 482, 3288  
 Hopkins, P. F., Hernquist, L., Cox, T. J., et al. 2005, ApJ, 630, 705  
 Hopkins, P. F., Hernquist, L., Cox, T. J., et al. 2006, ApJS, 163, 1  
 Hopkins, P. F., Hernquist, L., Cox, T. J., & Kereš, D. 2008, ApJS, 175, 356  
 Im, M., Griffiths, R. E., & Ratnatunga, K. U. 1997, ApJ, 475, 457  
 Im, M., Lee, I., Cho, Y., et al. 2007, ApJ, 664, 64  
 Jun, H. D., Assef, R. J., Carroll, C. M., et al. 2021, ApJ, 906, 21  
 Kaspi, S., Smith, P. S., Netzer, H., et al. 2000, ApJ, 533, 631  
 Khrykin, I. S., Hennawi, J. F., Worsack, G., et al. 2021, MNRAS, 505, 649  
 Kim, D., Im, M., & Kim, M. 2010, ApJ, 724, 386  
 Kim, D., Im, M., Glikman, E., et al. 2015a, ApJ, 812, 66  
 Kim, D., Im, M., Kim, J. H., et al. 2015b, ApJS, 216, 17  
 Kim, Y., Im, M., Jeon, Y., et al. 2015, ApJ, 813, L35  
 Kim, D. & Im, M. 2018, A&A, 610, A31  
 Kim, D., Im, M., Canalizo, G., et al. 2018, ApJS, 238, 37  
 Kim, Y., Im, M., Jeon, Y., et al. 2019, ApJ, 870, 86  
 Kim, D., Im, M., Kim, M., et al. 2020, ApJ, 894, 126  
 Kim, Y., Im, M., Jeon, Y., et al. 2020, ApJ, 904, 111  
 Kim, D., Lee, D., & Im, M. 2022, MNRAS, 509, 1147  
 Kim, Y., Im, M., Jeon, Y., et al. 2022, AJ, 164, 114  
 Kim, D., Im, M., Kim, M., et al. 2023, ApJ, 954, 156  
 Kim, D., Im, M., Lim, G., et al. 2024, Journal of Korean Astronomical Society, 57, 95  
 Kim, Y., Kim, D., Im, M., et al. 2024, arXiv:2408.03228  
 Krawczyk, C. M., Richards, G. T., Mehta, S. S., et al. 2013, ApJS, 206, 4  
 Lacy, M., Storrie-Lombardi, L. J., Sajina, A., et al. 2004, ApJS, 154, 166  
 Landt, H., Ward, M. J., Peterson, B. M., et al. 2013, MNRAS, 432, 113



- Lansbury, G. B., Banerji, M., Fabian, A. C., et al. 2020, MNRAS, 495, 2652
- Lasker, B. M., Lattanzi, M. G., McLean, B. J., et al. 2008, AJ, 136, 735
- Lee, I., Im, M., Kim, M., et al. 2008, ApJS, 175, 116
- Lyke, B. W., Higley, A. N., McLane, J. N., et al. 2020, ApJS, 250, 8
- Markwardt, C. B. 2009, Astronomical Data Analysis Software and Systems XVIII, 411, 251
- McLure, R. J., & Dunlop, J. S. 2004, MNRAS, 352, 1390
- Menci, N., Cavaliere, A., Fontana, A., et al. 2004, ApJ, 604, 12
- Pâris, I., Petitjean, P., Aubourg, É., et al. 2014, A&A, 563, A54
- Pâris, I., Petitjean, P., Aubourg, É., et al. 2018, A&A, 613, A51
- Planck Collaboration, Ade, P. A. R., Aghanim, N., et al. 2016, A&A, 594, A13
- Polletta, M., Weedman, D., Hönig, S., et al. 2008, ApJ, 675, 960-984
- Puchnarewicz, E. M., & Mason, K. O. 1998, MNRAS, 293, 243
- Rakshit, S., Stalin, C. S., & Kotilainen, J. 2020, ApJS, 249, 17
- Richards, G. T., Lacy, M., Storrie-Lombardi, L. J., et al. 2006, ApJS, 166, 470
- Risaliti, G., & Elvis, M. 2005, ApJ, 629, L17
- Rose, M., Tadhunter, C. N., Holt, J., & Rodríguez Zaurín, J. 2013, MNRAS, 432, 2150
- Rose, M. 2014, American Astronomical Society Meeting Abstracts #223, 223, #321.03
- Runnoe, J. C., Brotherton, M. S., & Shang, Z. 2012, MNRAS, 422, 478
- Sanders, D. B., Soifer, B. T., Elias, J. H., et al. 1988, ApJ, 325, 74
- Sanders, D. B., & Mirabel, I. F. 1996, ARA&A, 34, 749
- Schneider, D. P., Hall, P. B., Richards, G. T., et al. 2005, AJ, 130, 367
- Shen, Y., Richards, G. T., Strauss, M. A., et al. 2011, ApJS, 194, 45
- Shen, Y., Hall, P. B., Horne, K., et al. 2019, ApJS, 241, 34
- Shin, S., Im, M., Kim, Y., et al. 2020, ApJ, 893, 45
- Shin, S., Im, M., Kim, Y., et al. 2022, Journal of Korean Astronomical Society, 55, 131
- Skrutskie, M. F., Cutri, R. M., Stiening, R., et al. 2006, AJ, 131, 1163
- Stacey, H. R., Costa, T., McKean, J. P., et al. 2022, MNRAS, 517, 3377
- Suh, H., Civano, F., Hasinger, G., et al. 2019, ApJ, 872, 168
- Tozzi, P., Gilli, R., Mainieri, V., et al. 2006, A&A, 451, 457
- Urrutia, T., Lacy, M., & Becker, R. H. 2008, ApJ, 674, 80-96
- Urrutia, T., Becker, R. H., White, R. L., et al. 2009, ApJ, 698, 1095
- Urrutia, T., Lacy, M., Spoon, H., et al. 2012, ApJ, 757, 125
- Urry, C. M. & Padovani, P. 1995, PASP, 107, 803
- Vestergaard, M. 2002, ApJ, 571, 733
- Vestergaard, M. & Peterson, B. M. 2006, ApJ, 641, 689
- Véron-Cetty, M.-P., & Véron, P. 2006, A&A, 455, 773
- Virtanen, P., Gommers, R., Oliphant, T. E., et al. 2020, Nature Methods, 17, 261
- Webster, R. L., Francis, P. J., Petersont, B. A., Drinkwater, M. J., & Masci, F. J. 1995, Nature, 375, 469
- Weingartner, J. C. & Draine, B. T. 2001, ApJ, 548, 296
- Whiting, M. T., Webster, R. L., & Francis, P. J. 2001, MNRAS, 323, 718
- Wilkes, B. J., Schmidt, G. D., Cutri, R. M., et al. 2002, ApJ, 564, L65
- Wright, E. L., Eisenhardt, P. R. M., Mainzer, A. K., et al. 2010, AJ, 140, 1868
- Xu, D., Komossa, S., Zhou, H., et al. 2007, ApJ, 670, 60
- York, D. G., Adelman, J., Anderson, J. E., et al. 2000, AJ, 120, 1579
- Young, M., Elvis, M., & Risaliti, G. 2009, ApJS, 183, 17
- Zhou, H., Wang, T., Yuan, W., et al. 2006, ApJS, 166, 128